



Full length article

{10 $\bar{1}2$ } Twin interface structure and energetics in HCP materialsGorkem Gengor¹, Ahmed Sameer Khan Mohammed¹, Huseyin Sehitoglu*

Department of Mechanical Science and Engineering, University of Illinois at Urbana-Champaign, 105 S. Mathews Ave., Urbana, IL 61801, USA

ARTICLE INFO

Article history:

Received 16 June 2021

Revised 20 July 2021

Accepted 14 August 2021

Available online 19 August 2021

Keywords:

Twinning

HCP

Lattice and Motif atoms

Atomistics

Fault energies

ABSTRACT

This study systematically analyzes the {10 $\bar{1}2$ } twin in Hexagonally Close Packed (HCP) materials. Despite several propositions over 50 years, the Twin Boundary (TB) structure and twinning mechanism remain a debated topic, precluding determination of twinning energy barriers. This debate is resolved via Crystallographic Analytical Methods (CAM), Molecular Statics (MS) simulations in HCP Ti and Density Functional Theory (DFT) calculation of the Generalized Planar Fault Energy (GPFE) curve for several HCP materials. The {10 $\bar{1}2$ } crystallographic plane is “corrugated” comprising of two non-coincident sub-planes of lattice-sites (L-plane) and motif-sites (M-plane), causing ambiguity in determining the TB structure. This study resolves this ambiguity by establishing an energy-minimizing lattice-offset between the twin and matrix. At this offset, the TB forms by relaxation of both sub-planes into coincidence on a common atomic plane. A crystallographic calculation of this offset is proposed, extendable to non-single-lattice structures, in general. The twinning mechanism is determined, obtaining a shear-shuffle partition clarifying the motion of lattice and motif atoms. Nudged Elastic Band (NEB) simulations verify the mechanism along with disconnection-mediated migration of the twin. The GPFE is calculated for the first time in literature, to the best of our knowledge, revealing energy barriers for twin nucleation and migration. An absence of correlation of the unstable twinning energy barrier against twinning shear, Burgers vector magnitude or cohesive energy is shown, emphasizing the irreplaceability of the calculated barriers for predictive twinning models. Thus, a thorough clarification of the {10 $\bar{1}2$ } twinning mode is proposed, converging on the correct TB structure, twinning mechanism and energy barriers.

© 2021 Acta Materialia Inc. Published by Elsevier Ltd. All rights reserved.

1. Introduction

Hexagonally Close-Packed (HCP) materials such as Magnesium, Titanium, and their alloys constitute structural materials possessing low density, high specific strengths and corrosion resistance. Consequently, they are widely used in the aerospace, automotive, biomedical domains and offer a promising test bed for the development of next-generation lightweight structural alloys [1–8]. Even though the HCP crystal structure is one of the three most common crystal structures in structural materials (apart from Face-Centered Cubic, FCC, and Body-Centered-Cubic, BCC), its modes of deformation exhibit higher complexity [9–12]. For a crystalline material to accommodate any general applied deformation, its parent crystal structure must offer a minimum of 5 independent deformation modes (Taylor-von Mises criterion) [13,14]. While the FCC/BCC cubic systems comfortably satisfy this criteria via a sufficient number of slip systems, this is not enabled in HCP. In addition to slip, twinning modes are necessitated. This is why HCP materials

vastly exhibit twinning under deformation consequently leading to pronounced strain-hardening response [15–18] and microstructure-sensitivity of fatigue response [19–21]. Furthermore, unlike the cubic systems which exhibit 1–2 common twinning modes, there are at least 7 different twinning modes in HCP materials [11,22–24].

The predominant twin system in HCP materials is the {10 $\bar{1}2$ } twinning mode [9,11,13,25–29] and has been an active subject of research, particularly in the past 2 decades [12,22,24,26,29–44]. A twinning mode is characterized by a set of five twinning elements defined by the classical theory of deformation twinning [39]. These five elements are composed of the twinning plane K_1 , twinning direction η_1 , the conjugate plane K_2 , the conjugate twinning direction η_2 , and twinning shear, s . The conjugate plane K_2 is the second crystallographic plane that remains undistorted after undergoing twinning shear (the first undistorted plane is the twinning plane K_1 itself). The fundamental twinning elements for the {10 $\bar{1}2$ } twin mode has been shown in Table 1 and illustrated in Fig. 1 where the c and a axis of HCP unit cell are also shown.

Despite several studies, there remain some discrepancies in the understanding of the structure of the $K_1 = \{10\bar{1}2\}$ TB, the mechanism of detwinning and the energy barriers associated with this mechanism. The current study begins with a comprehensive

* Corresponding author.

E-mail address: huseyin@illinois.edu (H. Sehitoglu).¹ Both authors contributed equally to this paper.

Table 1
Twinning elements of $\{10\bar{1}2\}$
twin mode (here $\gamma = c/a$).

K_1	$\{10\bar{1}2\}$
η_1	$\langle 10\bar{1}1 \rangle$
K_2	$\{\bar{1}012\}$
η_2	$\langle \bar{1}01\bar{1} \rangle$
s	$(\gamma^2 - 3)/\gamma\sqrt{3}$

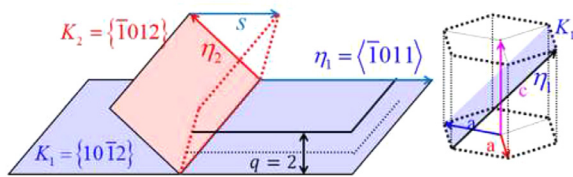


Fig. 1. Fundamental twinning elements of the $\{10\bar{1}2\}$ twinning mode: K_1 is the twinning plane, η_1 is the twinning direction, K_2 is the conjugate twinning plane, η_2 is the conjugate twinning direction and q is the minimum number of planes involved in the mechanism of twin migration; the HCP unit cell is also shown with the c and a axes, indicating the $\{10\bar{1}2\}$ plane within the cell.

overview of the prevalent discrepancies, exhaustively covering relevant literature, and aims to resolve them through a systematic determination of the structure, mechanism and energetics through Crystallographic Analytical Methods (CAM), Molecular Statics (MS) and Density Functional Theory (DFT) simulations. It is imperative to achieve such an understanding of this deformation mode in order to inform design of a new generation of lightweight structural materials comprising Ti-based alloys, Mg-based alloys and also the recently discovered HCP High Entropy Alloys (HEAs) [45–49].

1.1. Challenges in understanding of the $\{10\bar{1}2\}$ TB structure

Most understanding of TBs is derived from knowledge of cubic systems of FCC (primarily $\{111\}\langle 112 \rangle$ twinning) and BCC (primarily $\{112\}\langle 111 \rangle$ twinning) [23,50]. In cubic systems, TBs are common crystallographic planes between the matrix and twin variants that are related by a given orientation relation. This orientation relation is most often a mirror reflection implying that the TB plane is a mirror plane common between the two variants. Construction of the TB is straightforward as such a common plane can easily be found owing to the high symmetry of the cubic system (refer Figs. 2(a, b)). This plane is also known conventionally as the “coincident site boundary” [23]. It is worth mentioning that in BCC twins, although the TB structure is a common crystallographic $\{112\}$ plane, the twin resides at a slightly displaced position (an “offset”) from the matrix [51] as shown in Fig. 2(b). Thus there is a non-trivial “lattice offset” that exists between the twin and matrix. This lattice offset was determined only via atomistic simulation techniques and energy-minimization considerations [51] similar to those that will be employed in the current study. Nevertheless, both systems exhibit sufficient symmetry that allows the TB structure to be determined unambiguously as a common crystallographic plane between the twin and matrix.

In HCP structures some key challenges arise. While the basal and prismatic planes possess sufficient symmetry to allow TB construction similar to the cubic systems, the $\{10\bar{1}2\}$ plane is more complex. This crystallographic plane is not flat but “corrugated” in nature [11,22,26,33,52]. Therefore, the plane is composed of two non-coincident sub-planes henceforth denoted by L and M (Fig. 2(c)) planes. The L-plane is comprised of lattice site atoms and M-plane is comprised of atoms in the motif-site of the rhombohedral unit cell (Fig. 2(c)). The corrugation in the matrix and twin variants are not commensurate with each other and consequently, it is not as trivial to conceptualize a common TB similar

to the cubic systems. Several researchers have sought the structure within an atomistic simulation framework. The matrix and twin variants are constructed in their respective crystallographic orientations and allowed to relax, letting the atomistic framework find the energy-minimum TB structure relying on an empirical interatomic potential [22,26,30,42]. However the obtained structure is contingent on underlying assumptions related to the initial construction of the twin variants in the simulation (their relative positioning of the lattices) and dependent on the physical fidelity of the underlying potential. There needs to be a more fundamental crystallographic basis for constructing the TB and this basis has not been clarified to the best of the authors’ knowledge. Existing experimental evidence, primarily High-Resolution Transmission Electron Microscopy (HRTEM) has identified the existence of a sharp TB with a mirror-plane of atoms similar to the cubic structures [31–33, 43,53–55]. This plane does not exhibit the same corrugation that is expected from the crystallography of the $\{10\bar{1}2\}$ plane. Such a TB structure has also been an outcome of atomistic-scale simulations [22,26,30,42,56–58] somewhat inadvertently; it is not arrived at from a crystallographic derivation hence not well understood. This study explains the formation of the structure and the existence of a non-trivial lattice offset between the matrix and twin variants upon distinction of lattice (L) and motif (M) atoms. A close parallel to this problem was recently reported by the authors for B19’ NiTi monoclinic martensitic structures [59–61], and we adopt a similar methodology in this study.

We show in this study, that there is a variable known as the lattice offset which needs to be determined before the TB structure can be constructed within the atomistic framework. This offset, \bar{p} , defines the relative positioning of the twin lattice with reference to the matrix lattice and is often implicitly assumed to be zero. The importance of such an offset has been overlooked and only been shown in select cases till date, for instance the “Isoceles” twin in BCC structures mentioned above or in TBs of more complicated crystal structures [51,59]. In this study, atomistic simulations are employed to parametrically optimize the lattice offset in directions in-plane and normal to TB. We use energy-minimization considerations to find the correct offset yielding a unique energy-minimal TB structure. The underlying crystallographic basis for this offset value is proposed along with an analytical method to calculate it so that the TB structure can be constructed unambiguously circumventing atomistic simulations. Understanding of the TB structure precedes any study of the twinning mechanism as discussed below. This construction is further utilized to determine the stable TB energy values from ab initio DFT calculations en route to determining the complete Generalized Planar Fault Energy (GPFE) curve for all HCP metals analyzed in this study.

1.2. Challenges in understanding the $\{10\bar{1}2\}$ twinning mechanism

The mechanism of twinning refers to the set of atomic motions required to convert the matrix variant to the twin variant (or vice versa). For the highly symmetric cubic structures, the twinning mechanism is comprised purely by shear displacements without any shuffle [39]. In HCP however, the corrugated nature of the plane necessitates additional atomic motions apart from shear, henceforth referred to as “shuffles”. This adds a level of complexity in determination of the mechanism because several shear-shuffle combinations can be hypothesized to convert the matrix variant into its twin. And indeed several such propositions have been made over the past 5 decades [12,22,24,27,29,31,34–38, 41,42,44,57,62–64], only a select few of which are represented in Fig. 3. Notice that every proposition has a distinct mechanism. We classify the mechanisms based on 4 parameters:

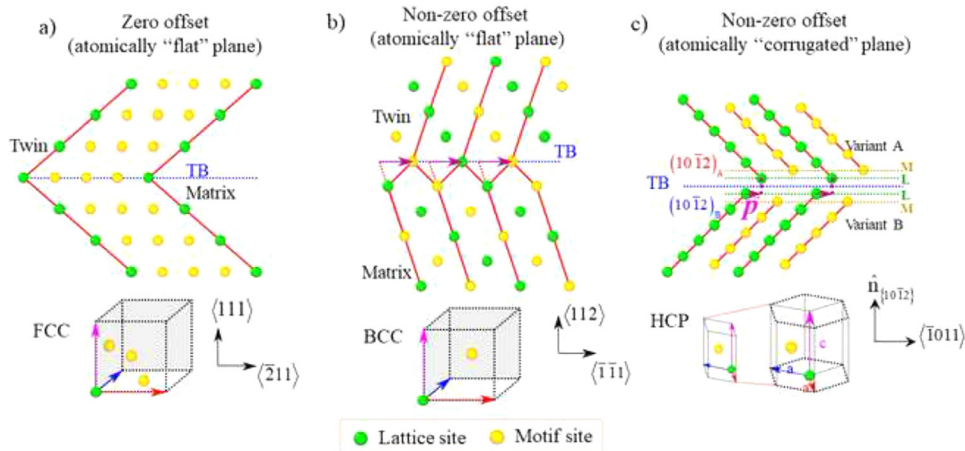


Fig. 2. Twin Boundary structures and lattice offsets: (a) {111} TBs in FCC materials are common crystallographic planes shared by the twin variants, with no lattice offset between the variants (b) “isocoles” {112} TBs in BCC materials are also common crystallographic planes but admit a lattice-offset \vec{p} between the lattices of the twin variants [23,51] (c) {10 $\bar{1}$ 2} TB structure is unclear as a common atomic-plane of atoms cannot be constructed owing to “corrugated” nature of the {10 $\bar{1}$ 2} plane in both variants; the corrugation is understood as a composite of two sub-planes – L-plane comprising lattice-site atoms and M-plane comprising motif site atoms; the lattice and motif sites are indicated in the cubic unit cells of FCC, BCC and rhombohedral unit cell of HCP; determination of lattice offset \vec{p} is critical to obtain the equilibrium TB structure. (For interpretation of the references to colour in this figure legend, the reader is referred to the web version of this article.)

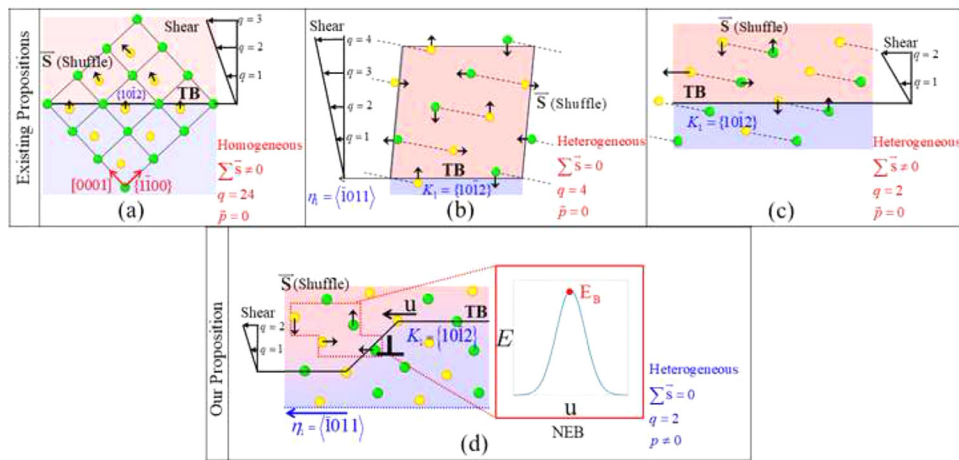


Fig. 3. Existing propositions of shear-shuffle detwinning mechanisms characterized based on 4 parameters: whether the mechanism is homogeneous (shear)/heterogeneous (dislocation-mediated), the number of planes involved (q), the net sum of shuffles ($\sum \vec{s}$) and lattice-offset between twin variants (\vec{p}) (a) Song and Gray [27,64] proposed a homogeneous instantaneous shearing of several planes, assuming zero lattice offset and non-zero sum of shuffles (b) Bevis and Crocker [24] proposed a heterogeneous mechanism based on classical theory with net zero sum of shuffles and unknown lattice offset (c) Wang et al. [22,42] improved to a 2-plane heterogeneous mechanism obtaining non-zero-sum of shuffles; (d) Our proposition establishes a heterogeneous 2-plane mechanism with net zero sum of shuffles arising from a precisely determined lattice offset vector; Nudged-Elastic Band (NEB) simulation is shown illustrating disconnection-mediated twin migration and corresponding energy barrier, E_B .

a Nature of twin nucleation and growth: There are two major categories corresponding to this nature, namely “homogeneous” and “heterogeneous” natures of twin nucleation and growth. Homogeneous twin nucleation and growth is achieved through instantaneous shearing and coordinated motion of a large region of matrix atoms, homogeneously, to form the twin. Contrastingly, heterogeneous twin nucleation and growth occurs at the local vicinity of certain line defects known as twinning disconnections and the sweeping motion of such disconnections across the matrix progressively achieves the twinning. While some of the earliest mechanisms were proposed to be homogeneous [64,65], it is now well-recognized that under nominal conditions (ambient temperature and pressure, low strain-rate of loading), the twinning mechanism is heterogeneous, mediated by disconnections. Based on atomistic potential-energy considerations, our study reaches the same conclusion through a Nudged Elastic Band (NEB) simulation.

b The lattice offset across the TB: As mentioned before, determination of the right equilibrium TB structure requires unambiguous determination of the lattice offset \vec{p} . Most studies implicitly assume it to be zero drawing from understanding of the simpler cubic structures (Fig. 2(a, b)). The deduced mechanism of twinning is sensitive to the equilibrium TB structure and in turn sensitive to the lattice offset parameter. In this study, the lattice offset is determined to be non-zero using atomistic simulation methods.

c Shear-Shuffle partitioning of the twinning mechanism: The twinning mechanism can be partitioned into atomic motions arising from the twinning shear and additional motions called “shuffles”. The twinning shear is one of the five fundamental twinning elements (Table 1) which can be derived from the crystallography of the matrix and twin lattices. However, the shuffles cannot be determined in the same way. Several distinct shear-shuffle partitions have been determined for the mechanism (refer figure 3). The classical theory stipulates a net zero

average shuffle for any twinning mechanism [24,39], but not all propositions agree with this condition [27]. It is imperative to determine the mechanism unambiguously so as to determine the energy barriers associated with the mechanism. This mechanism depends on the offset and the equilibrium TB structure. This study establishes the mechanism based on crystallographic and energetic considerations, verifying it within a Molecular Statics (MS) simulation framework.

- d The number of planes involved in the mechanism, q : This parameter is useful to quantify the complexity of the twinning mechanism in terms of how many minimum planes are involved. Classical theories defined this parameter based on crystallographic periodicity of the lattice obtaining a higher value of $q = 4$ [23,24,39]. More recently, topological theory defines this parameter based on a more reliable calculation of the twinning disconnection's Burgers vector, yielding a lower value $q = 2$ [37,53,54,66,67]. Our study verifies this value based on energetic degeneracy of different positions of the TB (MS and DFT simulations) and by Burgers vector calculations using the Topological Modeling (TM) framework.

It can be seen that all the proposed mechanisms summarized in Fig. 3 differ from each other based on at least one of the aforementioned parameters. Since the mechanism operates on a scale of few angstroms, no direct observations are available from an experimental standpoint, to the best of the authors' knowledge. Hence, the use of atomistic modeling techniques is necessitated as employed in this study. In the absence of a unique mechanism for twinning, energy barriers or critical stresses cannot be predicted unambiguously and will remain elusive. Several atomistic simulations focused on nucleation mechanisms, kinetic and morphological characteristics associated with the twin mode [22,25,26,30,42,43,57,68-73]. However it is necessary to obtain standardized energy barriers at a more fundamental scale, such as the Generalized Planar Fault Energy (GPFE). No such prediction has been made to the best of the authors' knowledge. And without reliable prediction of these energy barriers, critical twinning stresses cannot be predicted. Hence, it is necessary to resolve existing discrepancies in understanding of the twinning mechanism to approach calculation of these fundamental energy barriers, as is done in this study.

1.3. Approach of current study

In this study, we forward a systematic analysis to determine the $\{10\bar{1}2\}$ TB structure, detwinning mechanism and twinning energy barriers. Without any presumptions on the existence of a common mirror-plane, the equilibrium TB structure is constructed by positioning the twin variants at a specific lattice offset. This lattice offset is determined to be one which minimizes the potential energy as evaluated using Molecular Statics (MS). At this offset, volume-invariance of deformation twinning is upheld and it is shown that the corrugated plane (discussed in Section 1.2) relaxes into a common mirror-plane similar to the highly symmetric cubic systems (FCC/BCC). The mechanism of detwinning is determined, finding a shear-shuffle mechanism such that the net average shuffle is zero. This is verified in MS by establishing energetic degeneracy of the TB every two $\{10\bar{1}2\}$ planes instead of on every consecutive plane (as found in cubic systems FCC/BCC). The shear-shuffle mechanism is verified by a Nudged Elastic Band (NEB) simulation of twin migration. NEB verifies that the mechanism of twin growth is disconnection-mediated and the proposed shear-shuffle mechanism is observed at the disconnection front. The Burgers vector of the disconnection is obtained using principles of Topological Modeling (TM). The energetic degeneracy, shear-shuffle mechanism, NEB simulation and topological calculation of the Burgers vector authoritatively establish $q = 2$ for this twinning mode con-

sistent with [22,33,37,38,57,66,70]. Energy barriers for twinning are determined using ab initio Density Functional Theory (DFT) calculations of the Generalized Planar Fault Energy (GPFE) curve. This is done for the HCP materials: Ti, Mg, Zr, Zn, Cd, Be and Hf. The energy barriers of twinning for these twinning materials have not been provided before on this scale, to the best of the authors' knowledge. Hence, a thorough clarification of the structure, mechanism and energetics of twinning of the $\{10\bar{1}2\}$ twinning mode in HCP materials is proposed.

The need for understanding both the structure and mechanism to this depth is ultimately for ab initio determination of TB energy and energy barriers for twin nucleation/migration. For example, it is the clarity of both those features in cubic (FCC/BCC) systems that has led to the wealth of energy-barriers (stable and unstable twinning energies) available for them [11,74-82]. Consequently, they are leveraged in both analysis and design of new FCC/BCC alloys, for instance the modern FCC High Entropy Alloys (HEAs). With the increasing need for lightweight materials, it is imperative that we understand the structure and mechanism of $\{10\bar{1}2\}$ twinning in HCP materials to as much depth so that we can both predict and design energy barriers either favoring or preventing twinning deformation.

2. Modeling methodology and results

In this section, the atomistic approach to model the $\{10\bar{1}2\}$ TB structure and twinning mechanism in HCP materials is presented with Ti as the study target. Our methodology consists of sequential steps presented concurrently with the results of each step. This way of presenting is most effective to convey the methodology coherently, since the results of every step provide crucial information for the subsequent steps in the sequence. Atomistic simulations are performed within a Molecular Statics (MS) framework in LAMMPS [83] employing energy-minimization routines. The scientific interest on HCP materials in recent years led to many state-of-the-art interatomic potentials [84-89]. For Ti, the interatomic potential developed in [84] was chosen as it was fitted to fault energy signatures of inelastic deformation. This framework is sufficient to determine both the equilibrium structure and detwinning mechanisms. Additionally, the TB structure and shear-shuffle mechanism is derived from Crystallographic Analytical Methods (CAM). This approach is necessary as a prerequisite to DFT calculations for energy barriers, because it determines the correct atomic positions independent of any governing interatomic potential. Consequently, we incorporate the resulting structure and mechanism within an ab initio DFT framework to obtain more accurate predictions of the energetics of this twinning mode (TB energy and GPFE profile). We explain the MS and CAM methods below followed by the DFT calculations.

2.1. Structure of TB (MS)

Lattice constants consistent with the chosen potential are used, $a = 2.949 \text{ \AA}$ and $c = 4.698 \text{ \AA}$ found to be close to experimental measurements [90]. The rhombohedral unit cell of HCP crystal structure is described in Fig. 2(c) along with the conventional hexagonal cell. The unit cell contains two Ti atoms, one of which resides at $(0, 0, 0)$. This atom is termed as the lattice atom, while the other atom residing at $(\frac{1}{3}, \frac{2}{3}, \frac{1}{2})$ is termed as motif atom (see Fig 2(c)). The coordinates are expressed in Miller indices corresponding to the rhombohedral cell. In conventional HCP Miller-Bravais, the coordinates of the motif site are $(0, \frac{1}{3}, -\frac{1}{3}, \frac{1}{2})$ [9]. For the $\{10\bar{1}2\}$ twin, crystallographic relationship between the two twin variants is of mirror-symmetry classified as a "Type I" relationship by the definitions in the classical theory of twinning [39].

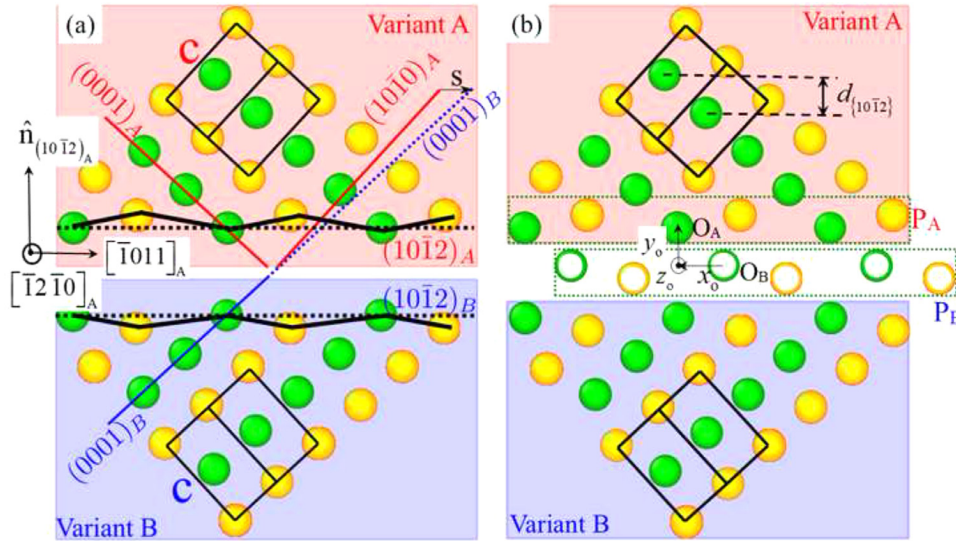


Fig. 4. Construction and analysis of TB within a Molecular Statics (MS) framework; (a) construction of twin variants following lattice orientation specified by Eqs. (1) and (2); (b) defining lattice offset as the difference vector (x_o, y_o, z_o) between reference origins O_A and O_B , chosen on crystallographic planes of variant A and B respectively.

Henceforth, the twin variant on the top will be designated as variant A, while the one at the bottom will be designated as variant B (refer Fig. 4). The lattice orientation of variant A is chosen such that the global $x-y-z$ axes of the LAMMPS simulation box are aligned as follows: $x||[\bar{1}011]_A$, $y||n_{\{10\bar{1}2\}_A}$ and $z||[\bar{1}2\bar{1}0]_A$. This orientation is more formally specified as a matrix C_A^{LAT} in which the columns represent the components of unit cell lattice vectors of the variants in the global reference frame. For the chosen orientation and the lattice constants this matrix can be calculated as:

$$C_A^{LAT} = \begin{pmatrix} -1.879 & 0 & 3.180 \\ 1.729 & 0 & 3.458 \\ -1.474 & 2.949 & 0 \end{pmatrix} \quad (1)$$

Given the lattice orientation of variant A, the lattice orientation of its twin i.e. variant B can be determined from the classical theory by applying mirror symmetry across the TB. This is given by the equation:

$$C_B^{LAT} = (I - 2(\hat{n} \otimes \hat{n}))C_A^{LAT} \quad (2)$$

where \hat{n} is the unit normal to the $\{10\bar{1}2\}$ TB. The initial twin structure is constructed as follows. A partitioning boundary is specified in the simulation box. The region below is populated with the crystal structure of variant B (Fig. 4(a)) and variant A is constructed in the region above. The lattice orientations specified by Eqs. (1) and (2) are followed.

2.2. Lattice offset (MS)

As mentioned in Section 1.1, the structures of the $(10\bar{1}2)_A$ and $(10\bar{1}2)_B$ crystallographic planes are corrugated and incommensurate with each other (refer Fig. 4). Thus the first objective is to resolve the equilibrium TB structure residing between the twin variants. In cubic structures such as FCC/BCC, the crystallographic planes in both variants have identical structure allowing the TB to be a common mirror plane between both variants. Determining this plane also fixes the relative positioning of the variant lattices across the TB. However, since such a common TB cannot be determined in the present case, the relative positioning of the variant lattices becomes a variable to be determined. This relative positioning is more formally defined as a lattice offset [59,61]. We determine this lattice offset first based on energy-minimization con-

siderations. Then the equilibrium TB structure is determined by relaxing the twinned structure at this offset within the MS framework.

First, the lattice offset must be defined. We define the lattice offset with the help of two atomic planes, i.e. P_A and P_B , shown in Fig. 4(b). P_A is an atomic plane of variant A immediately above the partition, while P_B is a virtual plane extending from variant B into variant A across the partition. In other words, P_B is where the next $(10\bar{1}2)_B$ plane of variant B would have been located if variant B structure was allowed to extend one plane above the partitioning boundary in the simulation box. Two arbitrary reference points are chosen on lattice-sites of both planes, O_A and O_B . The lattice offset vector is determined by the relative position of O_A with respect to O_B as (x_o, y_o, z_o) (refer Fig. 4(b)). If O_A and O_B coincide, the lattice offset is zero and the lattice sites of both variants coincide at on a common plane. We assert that this is most often assumed implicitly in early studies of this twin mode and that assumption is removed in the present study. Due to the periodic nature of HCP crystals, components of lattice offset vector exhibit periodicity. Therefore, it is natural to express them in normalized forms such as $0 \leq \bar{x}_o = x_o/|[\bar{1}011]| \leq 1$, $0 \leq \bar{y}_o = y_o/d_{\{10\bar{1}2\}} \leq 1$ and $0 \leq \bar{z}_o = z_o/|[\bar{1}2\bar{1}0]| \leq 1$. Here $d_{\{10\bar{1}2\}}$ is the interplanar spacing of the $\{10\bar{1}2\}$ planes. Throughout this paper, normalized lattice offsets will be denoted as \bar{x}_o , \bar{y}_o and \bar{z}_o , respectively.

First, we deduce the offset \bar{z}_o . It is well known that all atomic motions are constrained in the $(\bar{1}2\bar{1}0)$ plane. This plane is known as the plane of shear in the classical theory [39], which is normal to $z||[\bar{1}2\bar{1}0]$ direction. Consequently, the lattice of the twin and the matrix remain identical/coincident along this normal. This implies $\bar{z}_o = 0$. Fig. 5(a) illustrates the identity of structure of twin variants when viewed along $[\bar{1}2\bar{1}0]$ direction. Next, the component of the lattice offset normal to TB, \bar{y}_o , is determined. This is done by examining the interplanar distances across the partitioning boundary. For the lattice constants of the potential, the interplanar distance for $\{10\bar{1}2\}$ plane can be calculated as $d_{\{10\bar{1}2\}} = 1.729$ Å. This distance can be interpreted as the distance between consecutive L-L sub-planes or M-M sub-planes belonging to two consecutive $\{10\bar{1}2\}$ crystallographic planes as shown in Fig. 5(a). A fundamental property of deformation twinning is that it conserves the material volume. This implies that in transforming from the matrix (say, variant B) to the twin (respectively variant

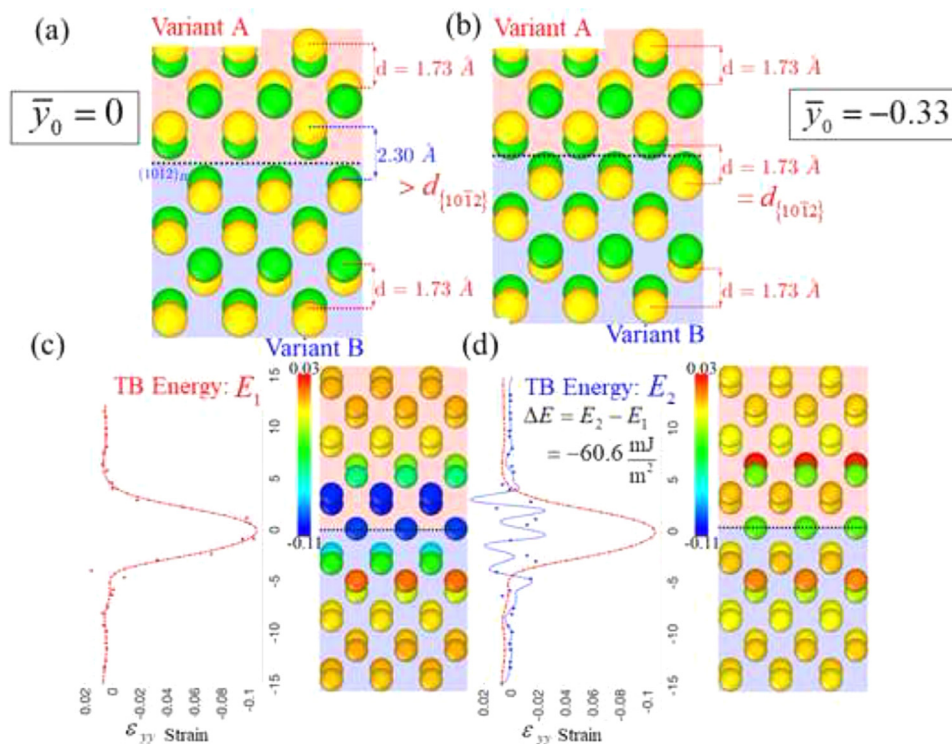


Fig. 5. Determination of lattice offset normal to the TB i.e. \bar{y}_0 : (a) Twinned structure, as viewed along $[\bar{1}011]_B$, at offset $\bar{y}_0 = 0$; the interplanar spacing across the TB is higher than the crystallographic spacing of $\{10\bar{1}2\}$ planes in the individual variants; (b) Twinned structure with non-trivial offset $\bar{y}_0 = -0.33$ conserving the interplanar spacing across the TB; (c) Variation of ϵ_{yy} strain component along y post energy-minimization of twinned structure in (a), indicating the presence of high compressive strain ($\sim 11\%$) at the TB; (d) Variation of ϵ_{yy} strain component post energy-minimization of twinned structure in (b), indicating the absence of significant strain and consequent lower TB energy by 60.6 mJ/m^2 (the strains in the atomic structure are calculated from discrete atomic displacements fitted to a Green-Lagrangian tensor, performed by OVITO [91]; the reference configuration for the strain-maps in (c) and (d) are (a) and (b) respectively).

A), the interplanar distances between the $\{10\bar{1}2\}$ planes must be preserved.

Fig. 5(a) and 5(b) show projections along twinning direction $(\bar{1}011)$ of unrelaxed TB structures constructed by using two different \bar{y}_0 values, 0 and -0.33 , respectively. When the TB was constructed by assuming $\bar{y}_0 = 0$, the interplanar separation across the TB is 2.31 \AA . This is higher than the nominal interplanar separation for $\{10\bar{1}2\}$ plane, $d_{\{10\bar{1}2\}}$. This implies that during twinning, there would have to be a volume-increase violating the volume-invariant condition of twinning. Hence, there must be a non-trivial $\bar{y}_0 \neq 0$ offset which preserves the spacing even across the partition. This offset is calculated to be $\bar{y}_0 = -0.33$.

We verify the energetic favorability of this non-trivial offset within the MS framework by performing an energy-minimization simulation. The simulation box is constructed as described in Section 2.1, having dimensions $69.4 \times 150.9 \times 8.8 \text{ \AA}^3$ (contains ~ 5200 atoms). Two twinned structures are constructed, with and without \bar{y}_0 offset respectively (refer Fig. 5(a) and 5(b)). Since the lateral directions $x||[\bar{1}011]_A$ and $z||[\bar{1}2\bar{1}0]_A$ are crystallographic, periodic boundary conditions are specified across them. Shrink-wrapped boundary conditions are enforced along $y||n_{\{10\bar{1}2\}A}$, with a “frozen” layer of atoms specified at the top and bottom ends along the direction. Within this layer, the atoms are constrained in the same position for the simulation. This is done with the notion that the atoms within these two layers are sufficiently far away to be unaffected by the equilibrium atomic relaxations at the vicinity of the TB. Hence, they would exhibit minimal deviation from the crystal structure of the respective variants. The width of the frozen layer is chosen as 10 \AA which is higher than the cutoff of the interatomic potential ($r_c = 6.9 \text{ \AA}$). In this manner, the atoms in the mobile region equilibrate under the influence of pure variant

crystal structures within the frozen layers far away from the TB. Given these boundary conditions, an energy-minimization simulation is carried out within MS employing the conjugate-gradient algorithm in LAMMPS [83]. The simulation terminates when the fractional energy change of the structure comes within the specified tolerance of 1.0×10^{-8} .

Fig. 5(c) and 5(d) illustrate local distribution of atomic strains in ϵ_{yy} direction after relaxation for $\bar{y}_0 = 0$ and $\bar{y}_0 = -0.33$ respectively. For the former case, normal atomic strains up to 11% to emerge. On the other hand, the structure with $\bar{y}_0 = 0.33$ exhibits ϵ_{yy} strains that are very nearly zero. The existence of higher local strains around the TB leads to higher TB energy due to addition of strain energy. The energy of the twin boundary without offset and with the right offset are determined to be $E_1 = 349.9 \text{ mJ/m}^2$ and $E_2 = 289.9 \text{ mJ/m}^2$ respectively. Hence, the calculated twin boundary energy difference between two structures is 60.6 mJ/m^2 favoring the structure with the non-trivial $\bar{y}_0 = -0.33$ offset. The prevalence of this offset in connection with TB energetics has not been revealed before to the best of the authors’ knowledge.

Finally, it is necessary to establish the lattice offset \bar{x}_0 parallel to the twinning direction $\hat{\eta}_1 = [10\bar{1}\bar{1}]_A$. There is no basis yet behind a specific choice for this offset, and typically it is presumed to be zero in the absence of any such basis. We establish its value by constructing twin structures with different \bar{x}_0 offsets systematically and calculating their potential energies within the MS framework under governance of the chosen potential [84]. The configuration with the lowest energy value determines the optimal lattice offset value. The results of this simulation have been reported in Fig. 6(a). As these results indicate, there are two candidates for optimal \bar{x}_0 offset: 0.0 and 0.45, determined with a discretization step size of 0.01 for \bar{x}_0 . Both structures are relaxed using the same boundary

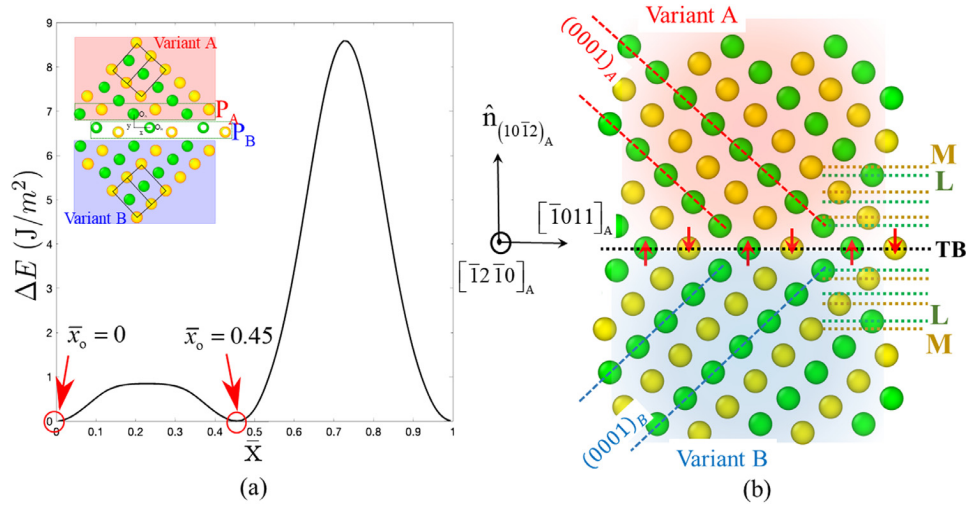


Fig. 6. Determination of lattice-offset \bar{x}_0 along twinning direction $\bar{\eta}_1$ (a) Configurational potential energy at varying offsets are determined from Molecular Statics (MS) simulations and the energy-minimizing offset values are determined (b) Relaxed TB structure illustrating the coincidence of lattice (L) and motif (M) planes at the TB and the corresponding local shuffle motions required for this formation of the TB; the TB forms as a common crystallographic plane between the twin variants similar to FCC/BCC cubic systems, however this structure is contingent on determining the right offset values. (For interpretation of the references to colour in this figure legend, the reader is referred to the web version of this article.)

conditions and conjugate-gradient scheme mentioned before. The relaxed TB structure at $\bar{x}_0 = 0$ is presented in Fig. 6(b), illustrating the local atomic motions which lead to the formation of the TB. At this offset, the incommensurate corrugation of the two variants are resolved at the TB by relaxing the L-plane and M-plane into coincidence. Consequently, a TB is formed as a common atomic-plane similar to the classical understanding of TBs in FCC and BCC structures. The structure at $\bar{x}_0 = 0.45$ shown is crystallographically identical to $\bar{x}_0 = 0$ in all respects with the only difference that the TB forms at a position one crystallographic plane above. The same atomic motions are followed exhibiting identical potential energy and TB atomic structure. Thus, without any loss in generality, the lattice offset of twin variant A with respect to twin variant B can be picked as either of the two candidate values and is chosen as $\bar{x}_0 = 0$ in the present study, thereby completing the triad $(\bar{x}_0, \bar{y}_0, \bar{z}_0) = (0, -0.33, 0)$. Notice that the lattice offset, as a vector is not trivial. And although the \bar{x}_0 component exhibits a trivial value, it must be determined as a result of the simulations proposed in this section and cannot be assumed a priori as was done in the past.

2.3. Crystallographic basis for determined offset – crystallographic analysis method (CAM)

The previous section determined the lattice offset based on atomistic energy (MS) considerations. In this section, a crystallographic basis for the determined offset is proposed, thereby proposing a method of construction that determines the offset without the need of atomistics. At this stage, we understand that the TB forms by atomic-motions that relax the L-plane and M-Plane of atoms into planar coincidence. The corresponding atomic motions are only normal to the TB. Furthermore, the TB forms as a common boundary between the two variants. The twin structure at zero-offset $(\bar{x}_0, \bar{y}_0, \bar{z}_0) = (0.0, 0.0, 0.0)$ is presented in Fig. 7(a). The origins O_A and O_B , at lattice sites of both variants, are coincident at $(0, 0, 0)$.

To calculate the lattice-offset vector, consider motif sites M_A and M_B on the corrugated planes P_A and P_B respectively (refer Figs. 4(b) and 7(a)). These motif sites must be related to each other by the twinning symmetry relation which in this case implies that one motif site, say M_A , is in the mirrored position of M_B , and vice

versa. The coordinates of both sites (with respect to chosen lattice origins O_A and O_B) can be determined as:

$$M_A = \bar{m}_A - [1\bar{2}10]_A; M_B = \bar{m}_B - [1\bar{2}10]_B \quad (3)$$

where $\bar{m}_A = [0, 1/3, -1/3, 1/2]_A$ and $\bar{m}_B = [0, 1/3, -1/3, 1/2]_B$ are the motif site positions within the unit cell of the respective lattices, expressed in Miller-Bravais indices. Switching to 3-component Miller indices, Eq. (3) can be re-written as:

$$M_A = \begin{bmatrix} 1 & 2 & 1 \\ 3 & 3 & 2 \end{bmatrix}_A - [110]_A = \begin{bmatrix} 2 & \bar{1} & 1 \\ 3 & 3 & 2 \end{bmatrix}_A$$

$$M_B = \begin{bmatrix} 1 & 2 & 1 \\ 3 & 3 & 2 \end{bmatrix}_B - [110]_B = \begin{bmatrix} 2 & \bar{1} & 1 \\ 3 & 3 & 2 \end{bmatrix}_B \quad (4)$$

Note that the subscripts A and B on the Miller-Bravais indices (Eq. (3)) and Miller indices (Eq. (4)) represent the crystallographic basis that the indices correspond to. Expressed in the global $x-y-z$ axes, we have

$$M_A = C_A^{\text{LAT}} \begin{pmatrix} -2/3 \\ -1/3 \\ 1/2 \end{pmatrix}; M_B = C_B^{\text{LAT}} \begin{pmatrix} -2/3 \\ -1/3 \\ 1/2 \end{pmatrix} \quad (5)$$

Now, the lattice offset must be such that the centroid of the lattice-motif pairs (O_A, M_A) and (O_B, M_B) must coincide. In other words we must have $(\frac{O_A + M_A}{2}) = (\frac{O_B + M_B}{2})$. Substituting $O_A = O_B + \bar{L}$ (Fig. 7(b)), the lattice-offset vector can be determined as:

$$\bar{L} = -\left(\frac{M_A - M_B}{2}\right) = \left(0, -d_{\{10\bar{1}2\}}/3, 0\right) \quad (6)$$

Following the normalization suggested in Section 2.2, we have the calculated lattice offset as

$$(\bar{x}_0, \bar{y}_0, \bar{z}_0) = \left(0, -1/3, 0\right) \quad (7)$$

consistent with the calculations of Section 2.2. The relaxed TB structure formed at this offset is shown in Fig. 7(c), same as that determined in Section 2.2 (Fig. 6(b)).

2.4. Mechanism of twinning: shear-shuffle partitioning (CAM)

The mechanism refers to the set of atomic motions required to convert one twin variant to the other i.e. to cause twinning. These

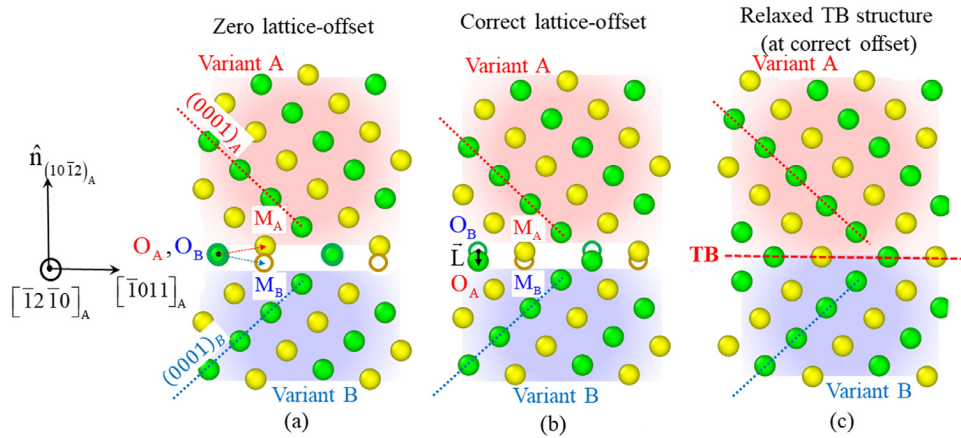


Fig. 7. Crystallographic basis for determined lattice offset: (a) Twinned structure at zero lattice offset, where both chosen origins coincide (b) Twinned structure at a non-trivial lattice offset \vec{L} (c) Energy-minimized TB structure at the determined lattice offset (TB energy is lower at the calculated non-trivial offset than a trivial/zero offset as discussed in Section 3).

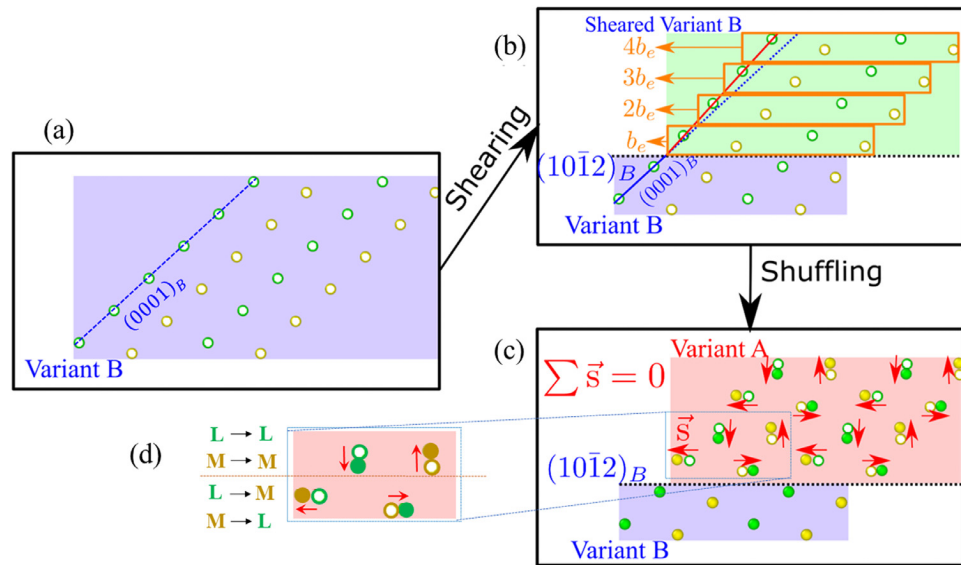


Fig. 8. Crystallographic determination of the twinning mechanism, specifically the shear-shuffle partitioning (illustrated on successive $\{10\bar{1}2\}$ planes) (a) Crystal structure of single-variant B ($(0001)_B$ basal plane indicated) (b) Shearing of single variant along twinning direction based on plane-by-plane displacements corresponding to Burgers vector $\vec{b}_e = sd_{\{10\bar{1}2\}}$ (note sheared position of basal plane) (c) Superposition of variant A crystal structure (filled circles) on sheared variant B configuration eliciting the shuffle motions required for twinning variant B into variant A (d) At the first $\{10\bar{1}2\}$ plane nearest to the TB (and every odd plane hence) there is a lattice (L)-to-motif (M) shuffle and vice versa; at the second $\{10\bar{1}2\}$ plane (and every even plane hence) the shuffles are lattice (L)-to-lattice (L) and motif (M)-to-motif (M). (For interpretation of the references to colour in this figure legend, the reader is referred to the web version of this article.)

atomic motions can be partitioned into motions corresponding to the twinning shear and additional shuffles which are independent of the shear. Since the twinning shear for $\{10\bar{1}2\}$ twin mode is theoretically established by the classical theory [23,39], the only difference between mechanisms stems from shuffling movements. Nevertheless, a complete understanding of the shuffling mechanism is necessary to setup Generalized Planar Fault Energy (GPFE) calculations with the appropriate constraints within DFT.

In this section, the mechanism is established from the crystallography of the individual twin variants. A two-step procedure is carried out. Starting from a pure variant, say variant B (refer Fig. 8(a)), twinning shear is applied to the region intended to form the twin variant. The twinning shear for this twin mode can be analytically calculated as $s = (\gamma^2 - 3)/\gamma\sqrt{3}$ along the direction $\hat{\eta}_1 = [10\bar{1}1]_B$, where $\gamma = c/a$. Using the lattice constants consistent with the interatomic potential of Ti, the shear is estimated to be $s = -0.167$ along $\hat{\eta}_1 = [10\bar{1}1]_B$, or equivalently $s = 0.167$ along

$\hat{\eta}_1 = [\bar{1}011]_B$. This shear is applied by enforcing rigid displacements of magnitude Nb ($N = 1, 2, 3, \dots$) along $\hat{\eta}_1$ at the Nth plane of the twin variant (refer Fig. 8(a, b)). Here b_e is the Burgers vector magnitude of the elementary twinning disconnection [23] which can be calculated as $b_e = sd_{\{10\bar{1}2\}}$. It is important to note that the shear is applied to the entire crystal structure i.e. on lattice and motif sites (or L-planes and M-planes). For the second step, the final structure of the twin variant is superposed onto this sheared variant (Fig. 8(c)). The shuffle motions are obtained as the atomic displacements required to transition from the sheared variant B to the final crystal structure of the twin variant A. It is also worth mentioning that in highly symmetric structures such as FCC/BCC, only the shear would be sufficient to complete twinning and the shuffle required would be zero. This is not the case in structures of lesser symmetry such as HCP or in martensitic structures [59]. Also, it can be seen that the shuffle motions depend on the exact position of variant A relative to variant B i.e. the lattice offset between the variants. Thus, determination of the energy-minimal

lattice offset, as done in Section 2.2 is critical to determine the correct mechanism of twinning. The required shuffle motions are shown in Fig. 8, and exhibits a periodicity of two $\{10\bar{1}2\}$ planes. In other words, $q = 2$ for this twinning mode, following the definition quoted in Section 1.2. It is also worth understanding the mechanism from the perspective of positional changes at the level of the unit cell. From Section 2.1, the atomic positions of the rhombohedral cell were assigned labels of lattice (L) and motif (M) positions, instrumental in understanding the corrugation and the formation of the TB structure (Figs. 6 and 7). Note that in the twinning mechanism, there are shuffles from the lattice site of the unit cell of the matrix to the motif site in the unit cell of the twin, and vice versa. This occurs on the first $\{10\bar{1}2\}$ plane adjacent to the TB, and on every odd plane hence. There are also shuffles where the lattice sites remain lattice sites in the twin with the same shuffle for motif sites as well. This occurs on the second $\{10\bar{1}2\}$ plane adjacent to the TB, and on every even plane hence. This mechanism will now be verified within the MS framework in the following section.

2.5. Nudged Elastic Band (NEB) simulation of twinning mechanism and twinning disconnection (MS)

Having established the mechanism crystallographically (CAM in Sections 2.3 and 2.4), we verify it by simulating TB migration in an atomistic framework. We continue with Ti as the study target, simulated under governance of the chosen interatomic potential. We first construct the TB at two distinct positions along the global $y||n_{\{10\bar{1}2\}_B}$ axis. The two positions are separated by two $\{10\bar{1}2\}$ planes. At both positions, the TB is independently constructed, determining the right offset following Section 2.2. The two twinned structures are then equilibrated/relaxed within MS, under the same boundary conditions as specified in Section 2.2. It is found that the TB energies at both positions are energetically degenerate. Thus, the TB is at a crystallographically equivalent position at every $\{10\bar{1}2\}$ plane separated by $2X$ planes from the initial TB position, where $X = 1, 2, 3$, etc. The minimum number of planes involved in the twinning mechanism for TB migration is that separating consecutively immediate energetically degenerate states equaling two, further confirming $q = 2$ for this twinning mode. A Nudged Elastic Band (NEB) simulation is used to determine the most energetically favorable transition between the two states, thereby determining the mechanism of twinning. It is worth noting that the simulation box dimensions are maintained to be the same at both states, as required in an NEB simulation. Only the atomic positions within the box are distinct by way of construction of the TB at different positions.

NEB has been commonly used to determine transition states in the same manner and the reader is referred to [92,93] for details of the algorithm. Briefly, the algorithm initializes a sufficient number of transition states or “replicas” to characterize the transition path between the two equilibrium states. An energy minimization is carried out on every replica by utilizing conjugate gradient method until the fractional change in force per atom converges within a tolerance of 0.1 eV/\AA . The results of NEB calculation are presented in Fig. 9, characterized by $N = 40$ replicas between (and inclusive of) the end-states. A low TB migration energy barrier has been obtained as $23 \frac{\text{mJ}}{\text{m}^2}$. Three different snapshots corresponding to three different replicas are extracted to illustrate the intermediate structural states. Positions $u_1 = 0$ and $u_3 \approx |b|$ correspond to states at the beginning and end of TB migration, respectively. The simulation finds a transition path between the end-states constituting a disconnection sweeping across the TB. This is illustrated in Fig. 9 observed at the peak position of the energy barrier (u_2) where a disconnection can be seen as a stepped TB. Furthermore, the simulation also yields the mechanism of twinning active at the

front of the disconnection core, illustrated in Fig. 9. Shuffle portion of atomic displacements has been identified by selecting a set of atoms that has been transformed from variant A into variant B and subtracting displacements corresponding to twinning shear from their total displacements. NEB calculation results have the following important implications:

- A heterogeneous disconnection-mediated mechanism is observed for twin migration in the $\{10\bar{1}2\}$ twin mode.
- The observed twinning disconnection has a characteristic step height of two $\{10\bar{1}2\}$ planes. This step height agrees well with the periodicity of the proposed twinning mechanism in Section 2.4, confirming $q = 2$ for this twinning mode.
- The observed shuffling displacements at Plane I and Plane II, occurring at the disconnection-front, are in good agreement with the predicted shuffling behavior in Section 2.3. Interpreting the shuffle movements on the scale of the unit cell, it can be seen that there are lattice-to-motif site shuffles on Plane I and lattice-to-lattice, motif-to-motif shuffles on Plane II. As disconnections sweep through the TB, atoms are sheared and shuffled to achieve twin migration.

The Burgers vector of the twinning disconnection is calculated using principles of Topological Modeling (TM) [60,67,94] Following TM, the Burgers vector can be calculated as the minimum difference of two translational symmetry vectors, one from variant B and another from variant A. It is given by:

$$\vec{b} = (\vec{r}_B - \vec{r}_A) \quad (8)$$

The translational symmetry vectors that yield a Burgers vector of least magnitude are $\vec{r}_B = [0001]_B$ and $\vec{r}_A = [\bar{1}010]_A$, illustrated in Fig. 10. Note that one vector lies on the basal plane of its twin (variant B) while the second vector lies on the prismatic plane of the other variant (variant A). This is consistent with prior understanding of $\{10\bar{1}2\}$ twinning where there is a prismatic-to-basal plane transformation during twinning. Here again, the step height of the disconnection can be calculated as,

$$h_D = \hat{n}_{\{10\bar{1}2\}} \cdot \vec{r}_B = 2d_{\{10\bar{1}2\}} \quad (9)$$

, yet again yielding $q = 2$ for the twinning mechanism. The calculated Burgers vector is also consistent with that obtained from classical theory, using the twinning shear:

$$\vec{b} = qsd_{\{10\bar{1}2\}} = 2\vec{b}_e = [0001]_B - [\bar{1}010]_A \quad (10)$$

A dichromatic complex [67,95] is constructed for the $\{10\bar{1}2\}$ TB and is shown in Fig. 10. This complex is essentially a superposition of atomic structures of the matrix and the twin, viewed on the plane of shear (the reader is referred to [67,95] for further details). The complex is constructed at the lattice offset established in Sections 2.2 and 2.3. It reveals the total atomic displacements required to convert one variant’s structure into that of its twin variant (variant A to variant B in Fig. 10). These displacements are partitioned into contributions from twinning shear and contributions from shear-independent shuffles.

2.6. Ab initio calculation of Generalized Planar Fault Energy (GPFE) landscape

At this juncture, the construction of the TB, the equilibrium TB structure, and the mechanism of detwinning have been established from both crystallographic considerations and Molecular Statics (MS) simulations. All results are necessary to obtain the Generalized Planar Fault Energy (GPFE) curve for the $\{10\bar{1}2\}$ twinning mode for several HCP metals. The GPFE curve captures the energy barrier required for nucleation of twins and growth/migration of the TB and is critical for the development of predictive models

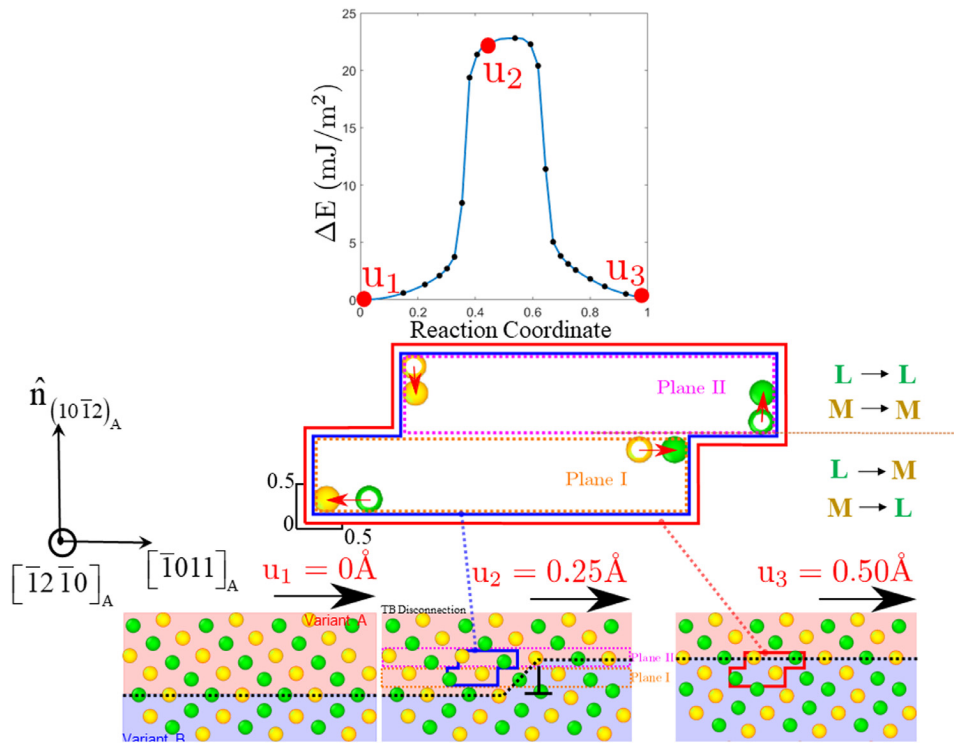


Fig. 9. Nudged Elastic Band (NEB) simulation of twin migration between two degenerate TB positions; the energy barrier across the transition states are determined by the simulation, select states of which are highlighted below; the transition states show a 2-plane disconnection sweeping along the TB causing twin migration; the mechanism of twinning at the disconnection front is the same as that established in Section 2.2 (Fig. 8(c)); the lattice-motif shuffles at each plane are also reiterated.

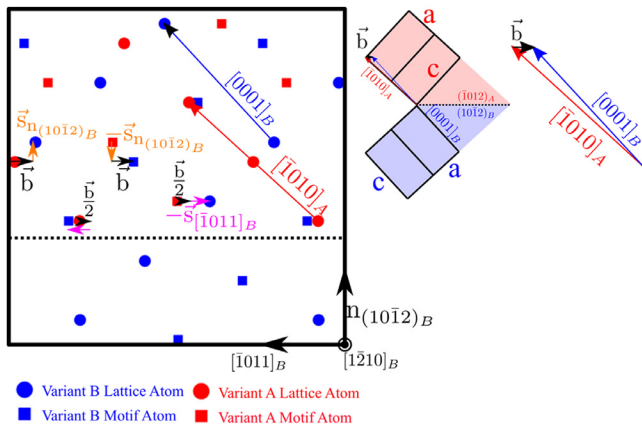


Fig. 10. Dichromatic Complex (DC) of the $\{10\bar{1}2\}$ twinning mode highlighting the translational symmetry vectors $[\bar{1}010]_A$ and $[0001]_B$ used to calculate the Burgers vector; the shear-shuffle partitioning of the twinning mechanism is also highlighted in the DC with shuffles perpendicular ($\vec{s}_{n_{1012}}$) and parallel ($\vec{s}_{\bar{1}011}$) to the twinning plane.

for twinning stresses devoid of any empiricism [11,74,75]. Only a brief description is provided here for convenience. The GPFE is calculated by starting from a single variant crystal structure and introducing a “disregistry” displacement u , successively on consecutive K_1 twinning planes. The disregistry is introduced by displacing one region of the crystal structure with respect to the other along the twinning direction, η_1 . The chosen plane across which the disregistry is introduced demarcates the two regions. Illustrated in Fig. 11(a) for a FCC crystal structure, a planar disregistry is first introduced on $K_1 = \{111\}$ plane A, then on plane B, and so forth until a twin region is formed within the single variant we started from. At each value of disregistry, u , the potential energy corresponding

to the atomic configuration is calculated from DFT, yielding a point on the GPFE curve corresponding to that u value. After introduction of sufficient disregistry, a twinned region is nucleated and two stable TBs are formed in the structure. Consequently, the GPFE curve exhibits a periodicity with the period equaling the magnitude of the Burgers vector of the twinning disconnection. This periodic region is referred to as the twin migration segment of the GPFE curve, and the region prior to twin migration is referred to as the twin-nucleation segment of the curve. Since all points on the curve are often determined using computationally intensive DFT simulations, it is generally sufficient to calculate critical points on the curve such as those corresponding to the unstable twinning energy barrier (γ_{ut}), and stable twin stacking fault (γ_{tsf}) energy (Fig. 12).

It must be emphasized that at each point on the curve corresponds to a DFT simulation of a distinct atomic configuration. And each simulation is an equilibration or ionic-relaxation of the structure under certain constraints. For simulation of highly-symmetric structures such as FCC, the only constraint to be enforced is that the atoms cannot relax along η_1 and only relaxations normal to the twinning direction are allowed. Furthermore as was discussed before in Section 1.1, sufficient symmetry is afforded by the structure to nucleate a twinned structure without requiring shuffling motions in the simulation. However, for the HCP structure, twinning requires considerable shuffle motions to be realized in the simulation (refer Fig. 11(b)). Further, shuffling movements along η_1 must be allowed as determined in Sections 2.4 and 2.5. All simulations in DFT are done with fully-periodic boundary conditions across all bounding planes of the simulation box. Details on construction of the single variant atomic structure and the periodic supercell are elaborated in Appendix A. Relaxations allowed along η_1 and other shuffling directions are discussed later in this section.

Thus, as shown in Fig. 11(b), the twin nucleation segment of the GPFE curve is calculated at select disregistries of $u = b, 2b, 3b$ with allowance of shuffles along η_1 in the disregistered region of the

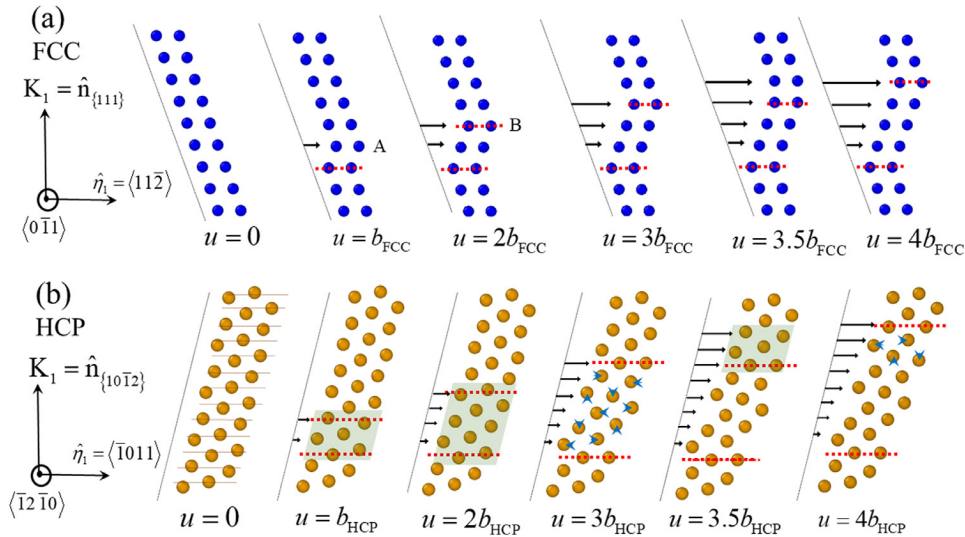


Fig. 11. Faulted atomic configurations used to determine the Generalized Planar Fault Energy (landscape): (a) Atomic structures for $\{111\}$ FCC twinning mode with $b_{\text{FCC}} = \frac{1}{6}\langle 112 \rangle$; the fault is first introduced on plane A, then plane B and so forth, nucleating a twinned region within the matrix; in the simulation all atoms are allowed to relax/equilibrate in all directions except the direction of twinning η_1 i.e. the direction in which the fault is introduced (b) Atomic structures for $\{10\bar{1}2\}$ twinning mode (where b_{HCP} is same as b calculated in Section 2.5); the atoms in the shaded translucent region are allowed to equilibrate/relax in all directions since shuffles in the direction of twinning/faulting must also be allowed; the required shuffle movements are highlighted by arrowheads at $u = 3b_{\text{HCP}}$ where two TBs form; the twin migration regime is calculated by introducing disregistry over the relaxed TB, accommodating the shuffle motions by allowing unconstrained equilibration/relaxation of atoms involved in the mechanism (up to two planes above since $q = 2$). (For interpretation of the references to colour in this figure legend, the reader is referred to the web version of this article.)

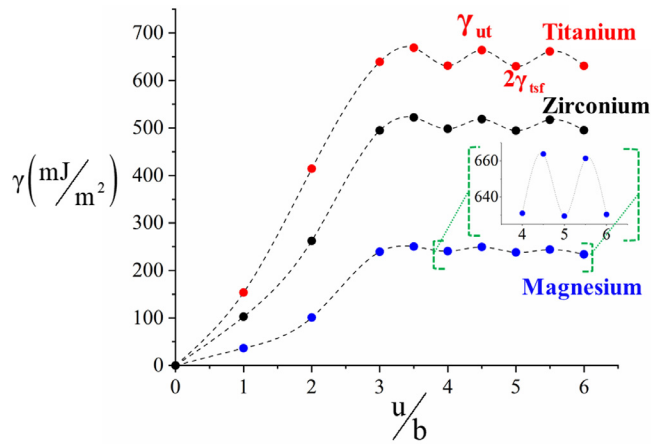


Fig. 12. Generalized Planar Fault Energy (GPFE) curve for select HCP metals: Titanium (Ti), Magnesium (Mg) and Zirconium (Zr) highlighting the critical points: unstable twinning energy barrier, γ_{ut} , at the peak of the curve and the stable minima representative of TB energy, γ_{tsf} .

structure. For example, at $u = 2b$, all atoms on the 4-planes within the shaded region indicated in Fig. 11(b) are allowed to relax in all directions, including along η_1 . Atoms on the remaining planes are constrained from moving along η_1 , while allowed to relax in both directions perpendicular to it. At $u = 3b$, we find that the energy of the disregistered configuration is higher than that for a twinned structure with 6 twinned planes. Thus at this point, a twin nucleus is energetically favorable, and henceforth from this point we only have twin migration. To calculate the twin-migration barrier, a disregistry is introduced 2 planes above the TB as shown in Fig. 11(b). The choice of 2-planes has to do with the fact that there are $q = 2$ planes involved in the twinning mechanism to migrate the TB (refer Section 2.4 and 2.5). A disregistry equaling $u = b/2$ is introduced from the twinned position, capturing the peak energy barrier departing from the stable TB. Atoms in these 2 planes are allowed to relax in all directions, including along η_1 . And as before,

atoms on remaining planes are constrained from moving along η_1 , while allowed to relax in both directions perpendicular to it. Thus, the GPFE for the $\{10\bar{1}2\}$ twinning mode in HCP materials is constructed by selective calculation of:

- Twin nucleation energy barrier at $u = 0, b, 2b$
- TB energy by constructing a twinned structure at $u = 3b, 4b, 5b, 6b$. This construction is based on the lattice-orientations and lattice-offsets from Sections 2.1-2.3. The calculated energies in DFT correspond to $2\gamma_{\text{tsf}}$ as shown in Fig. 12, corresponding to the formation of two stable TBs within the simulated supercell. Hence, the energy per unit area of the TB is given by γ_{tsf} , reported in Table 2.
- Unstable twinning energy barrier, γ_{ut} , at $u = 3b + b/2, 4b + b/2, 5b + b/2$ calculated by introducing disregistry on the stable twinned structures in (B). The average unstable energy across all the above positions are reported in Table 2.

A video of all equilibrated structures from simulations at each of the above configurations is presented as supplementary material (GPFE_Anim.mp4). The GPFE curve for Titanium, Magnesium and Zirconium is presented in Fig. 12. Results for all the HCP metals – Ti, Mg, Zr, Cd, Zn, Be, Hf are tabulated in Table 2. All simulations were performed in VASP [96,97]. The energy cut-off for electronic relaxations is chosen to be 1 milli-eV, and the force cut-off for convergence of ionic relaxation is selected as 5 meV/Å. There are additional details pertaining to DFT simulation such as size of simulation box (number of atoms), determination of plane-wave energy cut-offs, k-points, optimized lattice parameters, and shearing of the simulation box for maintenance of periodic boundary conditions. Discussion of these simulation details are deferred to Appendix A. In Table 2, the magnitudes of the Burgers vector, twinning shear and c/a ratio are based on lattice constants optimized for DFT calculations, as discussed elaborately in Appendix A. They closely agree with experimentally measured constants and are sufficient for the purposes of the study.

Table 2
Twinning characteristics of $\{10\bar{1}2\}$ twinning mode for HCP metals arranged in increasing order of twinning shear magnitude.

HCP metals	$\gamma = c/a$	Twinning shear magnitude s (Å)	Burgers vector magnitude $ b $ (Å)	Cohesive Energy per unit atom E_{coh} (eV)	Unstable twinning energy barrier γ_{ut} (mJ/m ²)	TB energy γ_{sf} (mJ/m ²)
Magnesium (Mg)	1.619	0.135	0.509	-1.506	247.4	118.9
Zirconium (Zr)	1.601	0.157	0.597	-8.458	518.9	247.8
Beryllium (Be)	1.587	0.175	0.463	-3.765	1351.5	649.7
Hafnium (Hf)	1.582	0.182	0.679	-9.960	897.2	429.8
Titanium (Ti)	1.580	0.185	0.63	-7.764	665.4	316.3
Zinc (Zn)	1.943	0.230	0.785	-1.108	263.0	131.0
Cadmium (Cd)	1.957	0.245	0.955	-0.745	75.6	36.1

3. Discussions

3.1. TB structure: lattice offsets (MS, CAM)

This study is focused on thorough clarification of crystallography, structure and twinning mechanism of the $\{10\bar{1}2\}$ twinning mode in HCP materials. This twinning mode is of significant interest due to its prominent role in mechanical response of lightweight HCP materials. Its influence on strain-hardening [15-18], fatigue [19-21] and fracture [98-100] have been studied extensively. At this stage of research, a complete understanding of the TB structure and twinning mechanistic has been missing to develop a predictive framework for the activation of this mode, in the form of twinnability [101-103] or Critical Resolved Shear Stress (CRSS) for twinning [75,76,104-106]. Such understanding is necessary to propel materials design of HCP alloys where a certain twinning propensity is intentionally engineered via tailoring of the chemistry, composition and microstructure. The advances made in FCC twinning after the development of such predictive models are testimonial to the potential benefit of developing an understanding to that depth [79].

The challenges in understanding the TB structure fundamentally comes from the corrugated nature of the $\{10\bar{1}2\}$ plane and fact that the corrugation is incommensurate between the two twin variants (refer Section 1.1 and Fig. 2). The origin of this corrugation can be traced back to the location of the motif site within the rhombohedral cell (Fig. 2). This position does not allow sufficient symmetry for the twinning plane to be atomically flat and leads to two distinct sub-planes: L-plane constituted by atoms on the lattice site and M-plane constituted by atoms on the motif site. This is unlike the convenience afforded in the cubic systems of FCC/BCC where the motif atoms within the unit cells are in highly symmetric positions, leading to coincidence of the L- and M- planes on a flat atomic plane. Consequently, a TB can be constructed as a coincident site boundary common between the two variants. However, this is not a trivial problem as it is prevalent in any crystal structure that is a non-single-lattice structure (i.e. has atleast one motif site atom apart from the lattice site within the unit cell) and possesses low symmetry e.g. martensitic structures of shape memory alloys that commonly exhibit internal twinning [59,61,107], twins or domain walls in ferroic materials [108,109] and minerals [110,111].

A common way to circumvent this challenge is to assume that the lattices of the twin variants are coincident on the twin boundary. In other words, the twin variants are constructed in their respective orientations and positioned such that only the lattice-site atoms are common at the TB. Such constructions were instrumental in studying this twin-mode within atomistic frameworks, either to analyze slip-twin interactions [73,112-114], to understand the nucleation of the twin mode from existing defects or to study kinetics of twinning behavior. While such a construction affords a good starting point and sufficient fidelity, it precludes the correct construction of the TB. This has strong implications on the TB energy that is an important physical parameter dictating the thermodynamic stability and twinnability of this mode. It also affects the calculation of the energetics of this twinning mode in DFT. In our approach, we take a step back and treat the relative position between the twin variant lattices as a variable, defined as the lattice offset vector \vec{p} . This concept is not new and has recently been applied to low-symmetry TBs in martensitic structures of Shape Memory Alloys [59] in our early studies. The challenges with HCP differ from the monoclinic case (where no such corrugations exist). The prevalent assumption of coincident lattice-sites on the TB, interpretable as zero lattice offset ($\vec{p} = 0$) is removed in our study. Instead a non-trivial lattice offset $\vec{p} \neq 0$ is determined unambiguously on the basis of volume-invariance of

deformation twinning and atomistic potential energies. It explains the formation of a common TB by relaxation of the L-plane and M-plane into coincidence. Such a common plane has been observed in high-resolution electron microscopy [31–33, 43,53–55] and in prior atomic-scale simulations [22,26,30,42,56,57] but no supporting justification or explanation has been provided to date. Such a justification is necessary to progress understanding of the twinning mechanism and corresponding twinning energy barriers. Furthermore, in the absence of lattice-offset, the energy of the TB is over-estimated significantly. For instance, in the case of Ti, the predicted TB energy in the absence of lattice offset would be over 20% higher than in the presence of the right lattice offset ($\Delta E \approx 60 \text{ mJ/m}^2$ and $E_2 \approx 289.9 \text{ mJ/m}^2$) as determined in Section 2.2). Such discrepancies will affect the accuracy of any predictive framework for twinning stresses. Also the proposed formation of the equilibrium TB structure removes the preferential treatment given to the coincidence of the lattice-sites over the motif-sites when considering that both atoms are same in all physical respects. We further propose a method to determine this offset crystallographically (the CAM framework). A pervasive implication of this approach is that equilibrium TB structures can be determined by such an approach for twins in several non-single-lattice structures in general.

3.2. Twinning mechanism: periodicity, disconnection step height and net shuffle (MS, CAM)

Determining the right lattice offset is instrumental for determining the right twinning mechanism. It is probable that because of the ambiguity associated with this offset that multiple mechanisms have emerged in the past [12,22,27,29,31,34–38, 41,42,44,57,62–64], some of which are summarized in Fig. 3 (a–c). Further this is associated with a lack of clarity about the minimum number of planes involved in the mechanism (alternatively the “periodicity” of the mechanism), given by the magnitude of q . The earliest propositions observed a periodicity of 24 planes (i.e. $q = 24$) in the twinning mechanism based on an assumed choice of the matrix and twin structures with zero lattice offset [27,64]. Subsequent propositions based the prediction on a crystallographic calculation of q . For a reflection twin, as in this case, it is defined as the number of $K_1 = \{10\bar{1}2\}$ planes intersecting a “primitive” lattice vector along $\hat{\eta}_2 = \langle \bar{1}01\bar{1} \rangle$ [23, 39], which in this case is $[\bar{1}01\bar{1}]$ itself. Such a calculation yields $q = 4$ for the twinning mode. Modern topological theory improved on both propositions to determine the smallest twinning disconnection Burgers vector \vec{b} . This Burgers vector is determined based on a fundamental property which is a break in translational symmetry in transitioning from the matrix to the twin, expressed in Eqs. (8) and (10) in this paper. Consequently, the periodicity of the mechanism is determined by the step height of the disconnection as $q = h_D/d$, which for the $\{10\bar{1}2\}$ TB yields $q = h_D/d_{\{10\bar{1}2\}} = 2$ (from Eq. (9), calculating $h_D = 3.458 \text{ \AA}$, twice of $d_{\{10\bar{1}2\}} = 1.729 \text{ \AA}$). In this approach, the magnitude of q is verified from multiple standpoints. First the periodicity of the shuffle motions is proposed in Section 2.4. Then it is found that the TB exhibits energetic degeneracy after two $\{10\bar{1}2\}$ planes in Section 2.5. The mechanism of TB migration is simulated using NEB, validating the number of planes involved as $q = 2$. Finally, a topological calculation is also used to determine the magnitude of the disconnection step height h_D , confirming $q = h_D/d_{\{10\bar{1}2\}} = 2$, as discussed above.

In determining the mechanism, the role of lattice offset is crucial as the lattice offset determines the relative positions of the twin variants, thereby determining the beginning and end atom positions to twin one variant into another. The twinning mechanism was determined crystallographically in Section 2.4 and then

from atomic-scale NEB simulations in Section 2.5. It was partitioned into shears and shuffles, illustrated in Figs. 8 and 9 and in the dichromatic complex in Fig. 10. We show that the net average shuffle associated with the mechanism is zero i.e. $\sum \vec{s} = 0$. This agrees with the tenets of the classical theory of deformation twinning [39]. We assert that a net zero shuffle is necessitated from a macroscopic standpoint as the only motions undergone by the material planes are exactly those corresponding to shear displacements. And these shear displacements are obtained from the twinning shear s which is a fundamental twinning element derivable from crystallography, independently of the twinning mechanism (refer Table 1). There can be no further movement of material associated with the shuffle component of the twinning mechanism [24,37]. If the net shuffle movements of atoms are non-zero i.e. $\sum \vec{s} = \vec{s}_{\text{net}} \neq 0$, then there is an additional rigid displacement that the material planes have effectively undergone during twinning. It would contradict the crystallography and hence cannot be admitted. In summary, we assert that any twinning mechanism, once partitioned into its shear and shuffle components requires $\sum \vec{s} = 0$, as was earlier proposed by the classical theory of twinning [24,38,39]. The critical consideration this study improves upon is the establishment of the right lattice offset which achieves the zero-shuffle condition exactly, building on their contribution. Furthermore, this study clarifies the lattice-to-motif shuffle exchanges (Figs. 8(d) and 9) at the fundamental level of the unit cell of the crystal. These exchanges emphasize the necessity to consider the motif atom position in equal footing as the lattice site to understand the TB structure and twinning mechanism, contrasting from a preferential consideration of lattice sites alone. Note that the current proposition establishes the best combination of parameters in the form of the smallest q , the absence of net shuffles i.e. $\sum \vec{s} = 0$ and energetically favored volume-conserving non-trivial lattice offset $\vec{p} \neq 0$, across all propositions of twinning made till date (Fig. 3). All these parameters were established unambiguously without empiricism and used to determine energy barriers for twinning.

An understanding of the TB structure and twinning mechanism to this detail is required to develop ab initio predictive models. And the first step in this direction is determination of the energy barriers for twinning, formalized by the Generalized Planar Fault Energy (GPFE) curve. Just as the Generalized Stacking Fault Energy (GSFE) curve formalizes the energy barriers associated with the motion of slip dislocations, and further instrumental in Peierls-Nabarro models for critical slip stresses [104,115], the GPFE is necessary to determine the critical twinning stresses, as was done for several FCC metals in [75,76,104–106]. The atomic structures must be established unambiguously as proposed in this study otherwise energetic predictions can be significantly off, as discussed previously in context of the lattice offset (energetic discrepancies as high as 20%). Further, knowledge of the mechanism is required to know the allowable constraints in equilibration of disregistered planar faults as done in Section 2.6. It is likely because of such complexities that no attempt to determine the GPFE has been made for this twin mode. Although a Generalized Stacking Fault Energy (GSFE) landscape has been determined [42] to formalize heterogeneous nucleation of the twin mode, the corresponding energy barriers and critical stresses required for this mechanism necessitate understanding of the fault energetics across multiple planes of twinning encompassed by the GPFE landscape.

3.3. GPFE landscape (DFT)

There is a lack of GPFE in HCP metals. For all HCP materials, it can be seen (Fig. 12 and Table 2) that the twin migration energy, given by $\gamma_{\text{TBM}} = (\gamma_{\text{ut}} - 2\gamma_{\text{tsf}})$ is significantly lower than the unstable twinning barrier γ_{ut} . This implies that majority of the energy barrier to twin in this mode goes into the formation of the stable

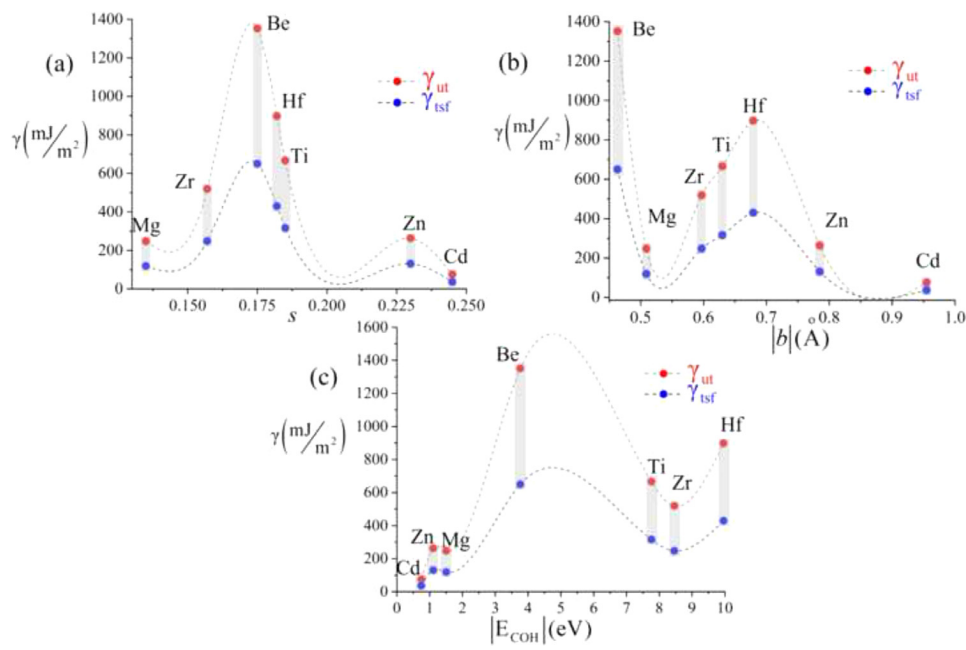


Fig. 13. Correlation between the unstable twinning energy barrier, γ_{ut} , and twin stacking fault energy (same as TB energy per unit area), γ_{tsf} , with (a) twinning shear, s , (b) Magnitude of twinning disconnection's Burgers vector, $|b|$, and (c) Cohesive energy per unit atom calculated from DFT, E_{COH} ; all correlations are poor indicating that no substitute to calculation of GPFE is, as of yet, available to predict twinnability or critical twinning stresses (the dashed lines are drawn as a fit to aid the eye). (For interpretation of the references to colour in this figure legend, the reader is referred to the web version of this article.)

twin boundaries and migration of these boundaries incurs a much lower cost. This explains the rapid migration of deformation twins post-nucleation earlier observed in mechanical tests [64,65]. Furthermore, this calculation allows us to check the correlation that is often drawn between the magnitude of twinning shear (or Burgers vector magnitude) and the twinning energy barrier. As can be seen in Fig. 13, there is not much correlation between the twinning shear or the Burgers vector magnitude with the magnitude of γ_{ut} (Fig. 13 (a,b)). The same goes with the cohesive energy (calculated as energy per atom, elaborated in Appendix A) which, despite being an energy measure for the HCP structure, does not explain the twinning energetics (Fig. 13(c)). Thus without a direct calculation of the fault energy landscape, assumptions about the energy barriers based on shear/Burgers vector magnitudes must be made with considerable caution. The calculated energy barriers will be instrumental in developing predictive models for $\{10\bar{1}2\}$ twinning mode in HCP materials, and further play an instrumental role in materials design of HCP alloy systems seeking to tailor the twinnability in this mode. They can also enrich semi-empirical potentials such as those developed in refs. [84–89], improving their capability to capture twinning and consequent material behaviors of HCP materials. To the best of the authors knowledge, an attempt of GPFE for a “corrugated” atomic structure has not been done before and would be instructive to determine GPFEs of other non single-lattice structures in general such as in martensites [59,61,107] or ferroic materials [108,109]. Therefore, this paper paves the way for further research in these materials.

Finally, we assert that the analysis framework developed in this study, can be readily extended to other twinning modes in HCP materials such as $\{10\bar{1}1\}$, $\{11\bar{2}1\}$ etc. [11,22–24]. Starting from construction of the lattices at the respective orientations in Section 2.1 and determination of the right lattice offsets using MS and CAM approaches (as elaborated in Section 2.2 and 2.3), one can establish the equilibrium TB structure for these twinning modes. The shear-shuffle mechanism can then be determined unambiguously using CAM approaches (Section 2.4) and simulated using NEB in an MS framework (Section 2.5). Ab initio energy bar-

riers can then be calculated following the proposed framework of DFT simulations elaborated in Section 2.6 and Appendix A. Thus, the framework developed in this study is pervasively applicable for other twinning modes in HCP materials allowing the development of predictive models for these modes without any empiricism.

4. Conclusions

This study proposes a thorough clarification of the TB structure and twinning mechanism of $\{10\bar{1}2\}$ twinning mode in HCP materials. Challenges associated with the corrugation of the twinning plane are addressed, and the TB structure is systematically constructed without invoking any empiricism. Having determined the relative lattice orientations based on classical theory of deformation twinning, the relative positions of the matrix and twin variants is treated as a variable, the lattice offset vector \vec{p} . The lattice offset is determined to be non-trivial based on considerations of atomistic potential energies and volume-invariance in twinning. The mechanism of twinning is crystallographically determined at this lattice offset. The mechanism is partitioned into shear and shuffle components, yielding a net zero average shuffle $\sum \vec{s} = 0$. Previous treatments violating this criteria have significant shortcomings. The twinning mechanism exhibits a periodicity of shuffle behavior every two planes indicative of $q = 2$ for this twinning mode. Shuffle movements have been shown to occur from lattice-to-motif positions, lattice-to-lattice positions and motif-to-motif positions within the two planes. Equilibrium TB structures at the calculated lattice offset are constructed and found to be energetically degenerate at separations of 2 planes. A Nudged Elastic Band (NEB) simulation is performed to simulate the mechanism of twinning between these degenerate positions, validating the shear-shuffle mechanism determined crystallographically and the magnitude of q . Under Molecular Statics (MS), the TB is found to migrate heterogeneously by motion of a twinning disconnection across the TB. The Burgers vector of the twinning disconnection is determined using Topological Modeling (TM) theory, obtained as a difference between two translational symmetry vectors in the ma-

trix and twin variants. The corresponding symmetry vectors validate the basal-to-prismatic plane transformation that has been commonly known to occur in this twinning mode. Finally, all information pertaining to the formation the TB, the lattice offset, and shear-shuffle mechanism are utilized to determine the Generalized Planar Fault Energy (GPFE) landscape for several HCP metals, calculated using ab initio Density Functional Theory (DFT). The complexities associated with the calculation of the GPFE are laid out explaining the lack of reported studies on the subject. It was found that the twin migration barrier for this twinning mode is considerable lower than the unstable twinning energy barrier for nucleating the twin. Further the calculated energy barriers do not correlate with either the magnitude of twinning shear or the magnitude of twinning disconnection's Burgers vector, emphasizing the necessity of calculated energy barriers to determine twinning propensities in different HCP materials. The understanding of TB structure, mechanisms and methods of determining energy barriers proposed in this study will ultimately be instrumental in design of HCP alloys with engineered twinning capabilities for superior mechanical behavior.

Declaration of Competing Interest

The authors declare that they have no known competing financial interests or personal relationships that could have appeared to influence the work reported in this paper.

Acknowledgment

We note that the authors G. Gengor and A.S.K. Mohammed contributed equally to this paper. The work is supported by Nyquist Chair funds which is gratefully acknowledged. The use of the Illinois Campus Cluster, a computing resource that is operated by the Illinois Campus Cluster Program (ICCP) in conjunction with the National Center for Supercomputing Applications (NCSA) and which is supported by funds from the University of Illinois at Urbana-Champaign, is also gratefully acknowledged.

Supplementary materials

Supplementary material associated with this article can be found, in the online version, at doi:10.1016/j.actamat.2021.117256.

Appendix A. DFT simulations required to calculate the Generalized Planar Fault Energy (GPFE) curve

An elaborate description of the construction of the simulation box and determination of DFT parameters for the GPFE calculation (Section 2.6) is presented here in detail, using Titanium (Ti) as an example. For the simulations, the pseudopotential with Projector Augmented Wave (PAW) basis wavefunctions and Perdew–Burke–Ernzerhof parametrization of Generalized Gradient Approximation (PBE-GGA) exchange correlation functional were employed [116]. The DFT parameters to be determined are the number of minimum k-points required in the simulation and the plane-wave energy cut-off. To determine them, self-consistent-field (SCF) simulations are run on the rhombohedral unit cell of the HCP crystal structure. The experimentally measured lattice constants (which for Ti are $a = 2.947 \text{ \AA}$ and $c = 4.704 \text{ \AA}$ [90]) are used to construct the 2-atom unit cell. The energy tolerance for convergence of the SCF calculation is specified to be 1 meV. The simulations are run at a series of increasing plane wave energy cut-offs and k-points, one at a time, results of which are shown in figures A1(a) and A1(b) respectively. The plane wave energy cut-off E_{CUT} is chosen to be the cut-off at which the relaxed energy is within a tolerance of 1 milli-eV. The value is found to be $E_{\text{CUT}} = 300\text{meV}$. The k-point cut-off is also chosen at the same tolerance, found to be $13 \times 13 \times 13$ for the unit cell. Next, the equilibrium lattice constants consistent with the chosen pseudopotential are to be determined. At the pre-determined DFT parameters, multiple self-consistent energy minimizations are run at a grid of values for a and c lattice constants. The optimal lattice constants are found to be $a = 2.925 \text{ \AA}$ and $c = 4.621 \text{ \AA}$, accurate to within $\pm 0.001 \text{ \AA}$, indicated in Fig. A1(c).

Having determined the lattice constants, a single twin variant crystal structure is constructed for the GPFE calculation. In DFT, all simulations of crystal structures are performed under fully periodic boundary conditions. Hence a supercell must be constructed with appropriate crystallographic directions as the bounding vectors of the supercell. The lattice vectors defining this periodic supercell are chosen to be $[\bar{1}011]$, $\frac{1}{3} \times [1\bar{2}10]$ and $4 \times [10\bar{1}2]$ (refer Fig. A2(a)). The multiplicative factors indicate the scale attached to 1 periodic distance along each lattice vector i.e. $[\bar{1}011]$, $[1\bar{2}10]$ and $[10\bar{1}2]$ respectively. In other words, the supercell has dimensions of 1 periodic distance along $[\bar{1}011]$, $\frac{1}{3}$ rd periodic distance along $[1\bar{2}10]$ and 4 times the periodic distance along $[10\bar{1}2]$. Periodic boundary conditions can be enforced across all boundaries

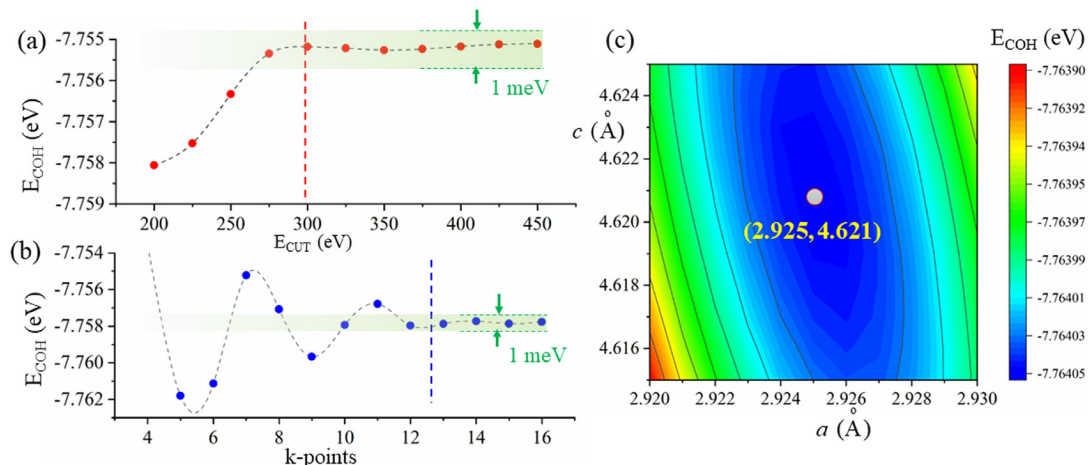


Fig. A1. Convergence calculations for DFT parameters (a) Plane wave energy-cut off E_{CUT} (taking $7 \times 7 \times 7$ k-points); the energy converges within a tolerance of 1 meV at $E_{\text{CUT}} = 300\text{eV}$ (b) Number of k-points (taking $E_{\text{CUT}} = 300\text{eV}$); the energy converges within tolerance of 1 meV at 13 k-points; (c) Determination of lattice constants optimal for the chosen pseudopotential.

Table A1
DFT simulation parameters for calculation of GPFE curve for HCP metals.

HCP metals	Experimental lattice constants (Å)	Optimized Lattice constants (Å)	Energy cutoff (eV)	k-Point mesh
Magnesium (Mg)	$a = 3.203$ $c = 5.199$ [117]	$a = 3.195$ $c = 5.174$	500	$15 \times 15 \times 1$
Zirconium (Zr)	$a = 3.233$ $c = 5.149$ [118]	$a = 3.230$ $c = 5.172$	500	$13 \times 13 \times 1$
Beryllium (Be)	$a = 2.281$ $c = 3.577$ [119]	$a = 2.258$ $c = 3.583$	375	$13 \times 13 \times 1$
Hafnium (Hf)	$a = 3.200$ $c = 5.061$ [120]	$a = 3.193$ $c = 5.050$	250	$12 \times 12 \times 1$
Titanium (Ti)	$a = 2.947$ $c = 4.704$ [90]	$a = 2.925$ $c = 4.621$	500	$13 \times 13 \times 1$
Zinc (Zn)	$a = 2.665$ $c = 4.947$ [121]	$a = 2.635$ $c = 5.120$	500	$15 \times 15 \times 1$
Cadmium (Cd)	$a = 2.972$ $c = 5.605$ [122]	$a = 3.008$ $c = 5.900$	500	$13 \times 13 \times 1$

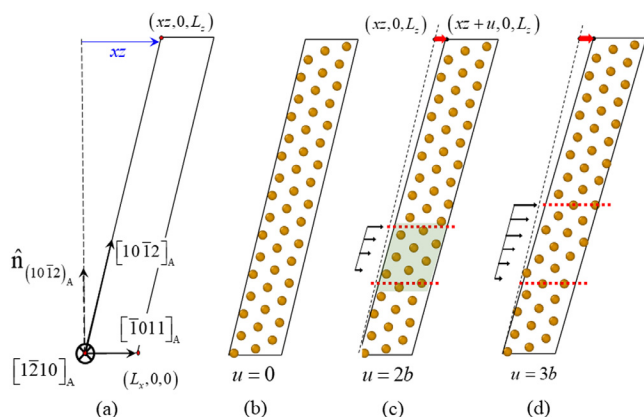


Fig. A2. Construction of simulation cell in DFT: (a) Monoclinic supercell along crystallographic directions; boundary conditions are periodic across all bounding planes (b) 48-atom supercell of a single-variant (say variant A) crystal structure (c) Disregistered position with $u = 2b$ with the thin arrows representing the planes on which disregistries have been introduced (also refer Fig. 11(b)); and the thick arrow represents the shear applied on the entire supercell to maintain periodic boundary conditions across the top and bottom xy planes (d) Relaxed structure at $u = 3b$ with nucleated twin variant in between the dashed lines (variant B). (For interpretation of the references to colour in this figure legend, the reader is referred to the web version of this article.)

of the supercell defined by these vectors, faithfully representing a single-variant crystal structure in HCP. The number of $(10\bar{1}2)$ planes intercepted by one periodic distance along $[10\bar{1}2]$ is 6, and hence the supercell considered in these simulations has 24 planes $(10\bar{1}2)$ planes. There are two atoms on each plane and hence the supercell contains 48 atoms.

To construct this supercell, the coordinates of the lattice vectors must be specified in a global x - y - z system. Assuming $x||[10\bar{1}1]$, we have $y||[1\bar{2}10]$ and $z||\hat{n}_{(10\bar{1}2)}$. Starting from the origin of the supercell, the coordinates of the end-points of the aforementioned lattice vectors can be determined to be of the form $(L_x, 0, 0)$, $(0, L_y, 0)$ and $(xz, 0, L_z)$ (refer Fig. A2(a)). Hence, we have a monoclinic supercell. For the calculated lattice constants for HCP Ti, we have: $L_x = 6.857 \text{ \AA}$, $L_y = 2.925 \text{ \AA}$, $xz = 9.940 \text{ \AA}$ and $L_z = 40.969 \text{ \AA}$. To construct the lattice, we follow Section 2.1 and specify the matrix C_A^{LAT} in which the columns represent the components of unit cell lattice

vectors of the variant in the global reference frame. For the chosen orientation and the lattice constants this matrix can be calculated as:

$$C_A^{LAT} = \begin{pmatrix} -1.872 & 0 & 3.114 \\ 1.463 & -2.925 & 0 \\ 1.707 & 0 & 3.414 \end{pmatrix} \quad (11)$$

The single variant crystal structure is created by populating the specified simulation supercell with the crystal structure whose lattice orientations are given by (11) and motif positions are given from Section 2.1. The filled simulation box is shown in Fig. A2(b) for reference. Starting from this structure, disregistries and constraints on atomic motion are introduced as discussed in Section 2.6. At each position of disregistry, an ionic-relaxation simulation is carried out within DFT. This simulation involves a series of self-consistent-field (SCF) calculations of electronic structure and then updation of ionic positions based on calculated forces on ions. The tolerance for energy convergence for SCF loops is specified as 1 meV, and the force tolerance for convergence is specified as 5 meV/atom. The energy cut-off is specified as 500 meV in accordance with the value calculated previously. The k-point mesh is specified as a Monkhorst-Pack k-point mesh grid of $13 \times 13 \times 1$ k-points. The optimized lattice constants, plane wave energy cutoff and k-point mesh used for DFT simulations of the GPFE curve for all HCP metals in this study are listed in Table A1. The cohesive energy per unit atom determined by unit cell simulations at the optimized lattice constants are also included.

The final aspect to consider is how periodicity across the supercell is retained as the disregistry is introduced. If a total disregistry equaling u is introduced within the supercell, then the simulation supercell is also sheared accordingly to maintain periodicity across the top and bottom $xy||[10\bar{1}2]$ planes (refer Fig. A2(c)). The shear is specified by changing the coordinates of the third lattice vector by an amount given by: $(xz, 0, L_z) \rightarrow (xz + u, 0, L_z)$ as indicated in the Fig. A2(c).

For potential energies in the nucleation regime ($u = 0, b, 2b$), the disregistry is introduced in the single variant structure according to Fig. 11. As noted in Section 2.6, at $u = 3b$, the energy of forming a 6-plane twin nucleus is preferred. The stable twinned structure is constructed by inserting variant B's crystal structure within variant A. The lattice orientation of variant B is given by Eqs. (11) and (2), with $\hat{n} = (0, 0, 1)$ in this case. Variant B's crystal structure must be constructed at normalized lattice

offset of $(\bar{x}_0 = x_0/|\bar{1}011|, \bar{y}_0 = y_0/|\bar{1}2\bar{1}0|, \bar{z}_0 = z_0/d_{\{10\bar{1}2\}} = -1/3)$. The energy cut-off for electronic relaxations is chosen to be 1 meV, and the force cut-off for convergence of ionic relaxation is selected as 5 meV/Å. The relaxed TB structure at $u = 3b$ is given in Fig. A2(d).

References

- G. Lütjering, J.C. Williams, in: Introduction, Titanium, Springer Berlin Heidelberg, Berlin, Heidelberg, 2007, pp. 1–14.
- B.L. Mordike, T. Ebert, Magnesium: properties – applications – potential, Mater. Sci. Eng. 302 (1) (2001) 37–45.
- M. Easton, A. Beer, M. Barnett, C. Davies, G. Dunlop, Y. Durandet, S. Blacket, T. Hilditch, P. Beggs, Magnesium alloy applications in automotive structures, JOM 60 (11) (2008) 57.
- J. Chen, L. Tan, X. Yu, L.P. Etim, M. Ibrahim, K. Yang, Mechanical properties of magnesium alloys for medical application: a review, J. Mech. Behav. Biomed. Mater. 87 (2018) 68–79.
- C.N. Elias, J.H.C. Lima, R. Valiev, M.A. Meyers, Biomedical applications of titanium and its alloys, JOM 60 (3) (2008) 46–49.
- A. Mehjabeen, T. Song, W. Xu, H.P. Tang, M. Qian, Zirconium alloys for orthopaedic and dental applications, Adv. Eng. Mater. 20 (9) (2018) 1800207.
- M.K. Kulekci, Magnesium and its alloys applications in automotive industry, Int. J. Adv. Manuf. Technol. 39 (9) (2008) 851–865.
- M. Peters, J. Kumpfert, C.H. Ward, C. Leyens, Titanium alloys for aerospace applications, Adv. Eng. Mater. 5 (6) (2003) 419–427.
- P.G. Partridge, The crystallography and deformation modes of hexagonal close-packed metals, Metall. Rev. 12 (1) (1967) 169–194.
- S. Mahajan, D.F. Williams, Deformation twinning in metals and alloys, Int. Metall. Rev. 18 (2) (1973) 43–61.
- I.J. Beyerlein, X. Zhang, A. Misra, Growth twins and deformation twins in metals, Annu. Rev. Mater. Res. 44 (1) (2014) 329–363.
- A. Ishii, J. Li, S. Ogata, Shuffling-controlled versus strain-controlled deformation twinning: the case for HCP Mg twin nucleation, Int. J. Plast. 82 (2016) 32–43.
- M.H. Yoo, Slip, twinning, and fracture in hexagonal close-packed metals, Metall. Trans. A 12 (3) (1981) 409–418.
- G. Lütjering, J.C. Williams, in: Fundamental Aspects, Titanium, Springer Berlin Heidelberg, Berlin, Heidelberg, 2007, pp. 15–52.
- D. Sarker, D.L. Chen, Detwinning and strain hardening of an extruded magnesium alloy during compression, Scr. Mater. 67 (2) (2012) 165–168.
- G.C. Kaschner, C.N. Tomé, R.J. McCabe, A. Misra, S.C. Vogel, D.W. Brown, Exploring the dislocation/twin interactions in zirconium, Mater. Sci. Eng. 463 (1) (2007) 122–127.
- A.A. Salem, S.R. Kalidindi, R.D. Doherty, Strain hardening of titanium: role of deformation twinning, Acta Mater. 51 (14) (2003) 4225–4237.
- Q. Ma, H. El Kadiri, A.L. Oppedal, J.C. Baird, B. Li, M.F. Horstemeyer, S.C. Vogel, Twinning effects in a rod-textured AM30 Magnesium alloy, Int. J. Plast. 29 (2012) 60–76.
- P.G. Partridge, Cyclic twinning in fatigued close-packed hexagonal metals, The philosophical magazine: a, J. Theoret. Exp. Appl. Phys. 12 (119) (1965) 1043–1054.
- K. Hazeli, H. Askari, J. Cuadra, F. Streller, R.W. Carpick, H.M. Zbib, A. Kotsos, Microstructure-sensitive investigation of magnesium alloy fatigue, Int. J. Plast. 68 (2015) 55–76.
- L. Wu, A. Jain, D.W. Brown, G.M. Stoica, S.R. Agnew, B. Clausen, D.E. Fielden, P.K. Liaw, Twinning–detwinning behavior during the strain-controlled low-cycle fatigue testing of a wrought magnesium alloy, ZK60A, Acta Mater. 56 (4) (2008) 688–695.
- J. Wang, J.P. Hirth, C.N. Tomé, $\{1\bar{0}12\}$ Twinning nucleation mechanisms in hexagonal-close-packed crystals, Acta Mater. 57 (18) (2009) 5521–5530.
- J.W. Christian, S. Mahajan, Deformation twinning, Prog. Mater. Sci. 39 (1) (1995) 1–157.
- A. Crocker, M. Bevis, in: The Crystallography of Deformation Twinning in titanium, The science, Technology and Application of Titanium, Elsevier, 1970, pp. 453–458.
- H. El Kadiri, C.D. Barrett, J. Wang, C.N. Tomé, Why are $\{10\bar{1}2\}$ twins profuse in magnesium? Acta Mater. 85 (2015) 354–361.
- C.D. Barrett, Analysis of twinning via automated atomistic post-processing methods, Philos. Mag. 97 (14) (2017) 1102–1128.
- A. Kelly, G.W. Groves, Crystallography and Crystal Defects, Addison-Wesley, Reading, Mass, 1970.
- M. Martinez, G. Fleurier, F. Chmelik, M. Knapek, B. Viguier, E. Hug, TEM analysis of the deformation microstructure of polycrystalline cobalt plastically strained in tension, Mater. Charact. 134 (2017) 76–83.
- B. Li, E. Ma, Atomic shuffling dominated mechanism for deformation twinning in magnesium, Phys. Rev. Lett. 103 (3) (2009) 035503.
- A. Luque, M. Ghazisaeidi, W.A. Curtin, A new mechanism for twin growth in Mg alloys, Acta Mater. 81 (2014) 442–456.
- J. Tu, S. Zhang, On the $10\bar{1}2$ twinning growth mechanism in hexagonal close-packed metals, Mater. Des. 96 (2016) 143–149.
- L. Li, S. Wang, L. Xiao, X. Chen, K. Wei, H. Ning, Y. Yu, D. Yin, H. Zhou, Atomic-scale three-dimensional structural characterisation of twin interface in Mg alloys, Philos. Mag. Lett. 100 (8) (2020) 392–401.
- S. Lay, G. Nouet, HREM study of the $\{0112\}$ twin interface in zinc, Philos. Mag. A 70 (2) (1994) 261–275.
- H. El Kadiri, C.D. Barrett, M.A. Tschopp, The candidacy of shuffle and shear during compound twinning in hexagonal close-packed structures, Acta Mater. 61 (20) (2013) 7646–7659.
- C. Cayron, Hard-sphere displacive model of extension twinning in magnesium, Mater. Des. 119 (2017) 361–375.
- R. Namakian, G.Z. Voyiadjis, An atomic displacive model for $10\bar{1}2\bar{1}011$ twinning in hexagonal close packed metals with the emphasis on the role of partial stacking faults in formation of $\{10\bar{1}2\}$ twins, Acta Mater. 150 (2018) 381–393.
- H.A. Khater, A. Serra, R.C. Pond, Atomic shearing and shuffling accompanying the motion of twinning disconnections in Zirconium, Philos. Mag. 93 (10–12) (2013) 1279–1298.
- A. Ostapovets, A. Serra, Review of non-classical features of deformation twinning in hcp metals and their description by disconnection mechanisms, Metals (Basel) 10 (9) (2020).
- B.A. Bilby, A.G. Crocker, A.H. Cottrell, The theory of the crystallography of deformation twinning, Proceed. Roy. Soc. Lond. Ser. A 288 (1413) (1965) 240–255.
- A. Ostapovets, P. Molnár, On the relationship between the “shuffling-dominated” and “shear-dominated” mechanisms for $\{10\bar{1}2\}$ twinning in magnesium, Scr. Mater. 69 (4) (2013) 287–290.
- S. Jiang, Z. Jiang, Q. Chen, Deformation twinning mechanism in hexagonal-close-packed crystals, Sci. Rep. 9 (1) (2019) 618.
- J. Wang, R.G. Hoagland, J.P. Hirth, L. Capolungo, I.J. Beyerlein, C.N. Tomé, Nucleation of a $\{1\bar{0}12\}$ twin in hexagonal close-packed crystals, Scr. Mater. 61 (9) (2009) 903–906.
- S. Wang, M. Gong, R.J. McCabe, L. Capolungo, J. Wang, C.N. Tomé, Characteristic boundaries associated with three-dimensional twins in hexagonal metals, Sci. Adv. 6 (28) (2020) eaaz2600.
- J. Wang, S.K. Yadav, J.P. Hirth, C.N. Tomé, I.J. Beyerlein, Pure-shuffle nucleation of deformation twins in hexagonal-close-packed metals, Mater. Res. Lett. 1 (3) (2013) 126–132.
- F. Brenne, A.S.K. Mohammed, H. Sehitoglu, High resolution atomic scale characterization of dislocations in high entropy alloys: critical assessment of template matching and geometric phase analysis, Ultramicroscopy 219 (2020) 113134.
- T. Nagase, M. Todai, T. Nakano, Development of Ti–Zr–Hf–Y–La high-entropy alloys with dual hexagonal-close-packed structure, Scr. Mater. 186 (2020) 242–246.
- C.L. Tracy, S. Park, D.R. Rittman, S.J. Zinkle, H. Bei, M. Lang, R.C. Ewing, W.L. Mao, High pressure synthesis of a hexagonal close-packed phase of the high-entropy alloy CrMnFeCoNi, Nat. Commun. 8 (1) (2017) 15634.
- Y.J. Zhao, J.W. Qiao, S.G. Ma, M.C. Gao, H.J. Yang, M.W. Chen, Y. Zhang, A hexagonal close-packed high-entropy alloy: the effect of entropy, Mater. Des. 96 (2016) 10–15.
- M.C. Gao, B. Zhang, S.M. Guo, J.W. Qiao, J.A. Hawk, High-entropy alloys in hexagonal close-packed structure, Metall. Mater. Trans. A 47 (7) (2016) 3322–3332.
- K.P.D. Lagerlöf, On deformation twinning in b.c.c. metals, Acta Metall. Mater. 41 (7) (1993) 2143–2151.
- P.D. Bristowe, A.G. Crocker, A computer simulation study of the structures of twin boundaries in body-centred cubic crystals, The Philosophical Magazine: a, J. Theoret. Exp. Appl. Phys. 31 (3) (1975) 503–517.
- N. Thompson, D.J. Millard, XXXVIII. Twin formation, in cadmium, Lond. Edinburgh Dublin Philosoph. Mag. J. Sci. 43 (339) (1952) 422–440.
- T. Braisaz, High-resolution electron microscopy study of the $\{10\bar{1}2\}$ twin and defects analysis in deformed polycrystalline alpha titanium, Philos. Mag. Lett. 74 (5) (1996) 331–338.
- T. Braisaz, P. Ruterana, G. Nouet, R.C. Pond, Investigation of $\{10\bar{1}2\}$ twins in Zn using high-resolution electron microscopy: interfacial defects and interactions, Philos. Mag. A 75 (4) (1997) 1075–1095.
- Q. Sun, X.Y. Zhang, Y. Ren, J. Tu, Q. Liu, Interfacial structure of $\{10\bar{1}2\}$ twin tip in deformed magnesium alloy, Scr. Mater. 90–91 (2014) 41–44.
- O. MacKain, M. Cottura, D. Rodney, E. Clouet, Atomic-scale modeling of twinning disconnections in zirconium, Phys. Rev. B 95 (13) (2017) 134102.
- M. Gong, J.P. Hirth, Y. Liu, Y. Shen, J. Wang, Interface structures and twinning mechanisms of twins in hexagonal metals, Mater. Res. Lett. 5 (7) (2017) 449–464.
- A. Ostapovets, A. Serra, Characterization of the matrix–twin interface of a $\{10\bar{1}2\}$ twin during growth, Philos. Mag. 94 (25) (2014) 2827–2839.
- A.S.K. Mohammed, H. Sehitoglu, Modeling the interface structure of type II twin boundary in B19' NiTi from an atomistic and topological standpoint, Acta Mater. 183 (2020) 93–109.
- A.S.K. Mohammed, H. Sehitoglu, Strain-sensitive topological evolution of twin interfaces, Acta Mater. 208 (2021) 116716.
- A.S.K. Mohammed, H. Sehitoglu, Martensitic twin boundary migration as a source of irreversible slip in shape memory alloys, Acta Mater. 186 (2020) 50–67.
- Y. He, B. Li, C. Wang, S.X. Mao, Direct observation of dual-step twinning nucleation in hexagonal close-packed crystals, Nat. Commun. 11 (1) (2020) 2483.

- [63] S. Jiang, T. Liu, L. Lu, W. Zeng, Z. Wang, Atomic motion in Mg–3Al–1 Zn during twinning deformation, *Scr. Mater.* 62 (8) (2010) 556–559.
- [64] S.G. Song, G.T. Gray, Structural interpretation of the nucleation and growth of deformation twins in Zr and Ti–I. Application of the coincidence site lattice (CSL) theory to twinning problems in h.c.p. structures, *Acta Metall. Mater.* 43 (6) (1995) 2325–2337.
- [65] S.G. Song, G.T. Gray, Structural interpretation of the nucleation and growth of deformation twins in Zr and Ti–II. Tem study of twin morphology and defect reactions during twinning, *Acta Metall. Mater.* 43 (6) (1995) 2339–2350.
- [66] A. Serra, D.J. Bacon, R.C. Pond, The crystallography and core structure of twinning dislocations in H.C.P. metals, *Acta Metall.* 36 (12) (1988) 3183–3203.
- [67] J.P. Hirth, R.C. Pond, Steps, dislocations and disconnections as interface defects relating to structure and phase transformations, *Acta Mater.* 44 (12) (1996) 4749–4763.
- [68] X.-Z. Tang, Q. Zu, Y.-F. Guo, The diffusive character of extension twin boundary migration in magnesium, *Materialia* 2 (2018) 208–213.
- [69] Y. Hu, V. Turlo, I.J. Beyerlein, S. Mahajan, E.J. Lavernia, J.M. Schoenung, T.J. Rupert, Embracing the chaos: alloying adds stochasticity to twin embryo growth, *Phys. Rev. Lett.* 125 (20) (2020) 205503.
- [70] Y. Hu, V. Turlo, I.J. Beyerlein, S. Mahajan, E.J. Lavernia, J.M. Schoenung, T.J. Rupert, Disconnection-mediated twin embryo growth in Mg, *Acta Mater.* 194 (2020) 437–451.
- [71] B. Xu, L. Capolungo, D. Rodney, On the importance of prismatic/basal interfaces in the growth of (11012) twins in hexagonal close packed crystals, *Scr. Mater.* 68 (11) (2013) 901–904.
- [72] J. Wang, I.J. Beyerlein, C.N. Tomé, An atomic and probabilistic perspective on twin nucleation in Mg, *Scr. Mater.* 63 (7) (2010) 741–746.
- [73] A. Serra, D.J. Bacon, A new model for {1012} twin growth in hcp metals, *Philos. Mag. A* 73 (2) (1996) 333–343.
- [74] S. Ogata, J. Li, S. Yip, Energy landscape of deformation twinning in bcc and fcc metals, *Phys. Rev. B* 71 (22) (2005) 224102.
- [75] S. Kibey, J.B. Liu, D.D. Johnson, H. Sehitoglu, Predicting twinning stress in fcc metals: linking twin-energy pathways to twin nucleation, *Acta Mater.* 55 (20) (2007) 6843–6851.
- [76] S.A. Kibey, L.L. Wang, J.B. Liu, H.T. Johnson, H. Sehitoglu, D.D. Johnson, Quantitative prediction of twinning stress in fcc alloys: application to Cu–Al, *Phys. Rev. B* 79 (21) (2009) 214202.
- [77] S. Kibey, J.B. Liu, M.J. Curtin, D.D. Johnson, H. Sehitoglu, Effect of nitrogen on generalized stacking fault energy and stacking fault widths in high nitrogen steels, *Acta Mater.* 54 (11) (2006) 2991–3001.
- [78] A. Ojha, H. Sehitoglu, L. Patriarca, H.J. Maier, Twin nucleation in Fe-based bcc alloys—Modeling and experiments, *Model. Simul. Mater. Sci. Eng.* 22 (7) (2014) 075010.
- [79] P. Chowdhury, H. Sehitoglu, Atomistic energetics and critical twinning stress prediction in face and body centered cubic metals: recent progress, *J. Eng. Mater. Technol.* 140 (2) (2018).
- [80] P. Chowdhury, H. Sehitoglu, H.J. Maier, R. Rateick, Strength prediction in NiCo alloys – The role of composition and nanotwins, *Int. J. Plast.* 79 (2016) 237–258.
- [81] A. Ojha, S. Alkan, L. Patriarca, H. Sehitoglu, Y. Chumlyakov, Shape memory behavior in Fe3Al—modeling and experiments, *Philos. Mag.* 95 (23) (2015) 2553–2570.
- [82] P. Andric, B. Yin, W.A. Curtin, Stress-dependence of generalized stacking fault energies, *J. Mech. Phys. Solid.* 122 (2019) 262–279.
- [83] S. Plimpton, Fast parallel algorithms for short-range molecular dynamics, *J. Comput. Phys.* 117 (1) (1995) 1–19.
- [84] M.I. Mendelev, T.L. Underwood, G.J. Ackland, Development of an interatomic potential for the simulation of defects, plasticity, and phase transformations in titanium, *J. Chem. Phys.* 145 (15) (2016) 154102.
- [85] Z. Wu, M.F. Francis, W.A. Curtin, Magnesium interatomic potential for simulating plasticity and fracture phenomena, *Model. Simul. Mater. Sci. Eng.* 23 (1) (2014) 015004.
- [86] M.S. Nitol, D.E. Dickel, C.D. Barrett, Artificial neural network potential for pure zinc, *Comput. Mater. Sci.* 188 (2021) 110207.
- [87] D. Dickel, D.K. Francis, C.D. Barrett, Neural network aided development of a semi-empirical interatomic potential for titanium, *Comput. Mater. Sci.* 171 (2020) 109157.
- [88] M.I. Mendelev, G.J. Ackland, Development of an interatomic potential for the simulation of phase transformations in zirconium, *Philos. Mag. Lett.* 87 (5) (2007) 349–359.
- [89] Y.-M. Kim, B.-J. Lee, M.I. Baskes, Modified embedded-atom method interatomic potentials for Ti and Zr, *Phys. Rev. B* 74 (1) (2006) 014101.
- [90] R.M. Wood, The lattice constants of high purity alpha titanium, *Proc. Phys. Soc.* 80 (3) (1962) 783–786.
- [91] A. Stukowski, Visualization and analysis of atomistic simulation data with OVITO—the Open Visualization Tool, *Model. Simul. Mater. Sci. Eng.* 18 (1) (2009) 015012.
- [92] G. Henkelman, H. Jónsson, Improved tangent estimate in the nudged elastic band method for finding minimum energy paths and saddle points, *J. Chem. Phys.* 113 (22) (2000) 9978–9985.
- [93] G. Henkelman, B.P. Uberuaga, H. Jónsson, A climbing image nudged elastic band method for finding saddle points and minimum energy paths, *J. Chem. Phys.* 113 (22) (2000) 9901–9904.
- [94] R.C. Pond, J.P. Hirth, K.M. Knowles, Topological model of type II deformation twinning in NiTi martensite, *Philos. Mag.* 99 (13) (2019) 1619–1632.
- [95] R.C. Pond, D.S. Vlachavas, J.W. Christian, Bicrystallography, *Proceed. Roy. Soc. Lond. A* 386 (1790) (1983) 95–143.
- [96] G. Kresse, J. Furthmüller, Efficient iterative schemes for ab initio total-energy calculations using a plane-wave basis set, *Phys. Rev. B* 54 (16) (1996) 11169–11186.
- [97] G. Kresse, D. Joubert, From ultrasoft pseudopotentials to the projector augmented-wave method, *Phys. Rev. B* 59 (3) (1999) 1758–1775.
- [98] B. Li, Q. Ma, Z. McClelland, S.J. Horstemeyer, W.R. Whittington, S. Brauer, P.G. Allison, Twin-like domains and fracture in deformed magnesium, *Scr. Mater.* 69 (6) (2013) 493–496.
- [99] D. Ando, J. Koike, Y. Sutou, The role of deformation twinning in the fracture behavior and mechanism of basal textured magnesium alloys, *Mater. Sci. Eng.* 600 (2014) 145–152.
- [100] V. Kaushik, R. Narasimhan, R.K. Mishra, Experimental study of fracture behavior of magnesium single crystals, *Mater. Sci. Eng.* 590 (2014) 174–185.
- [101] E.B. Tadmor, N. Bernstein, A first-principles measure for the twinnability of FCC metals, *J. Mech. Phys. Solids* 52 (11) (2004) 2507–2519.
- [102] B.Q. Li, M.L. Sui, S.X. Mao, Twinnability prediction for fcc metals, *J. Mater. Sci. Technol.* 27 (2) (2011) 97–100.
- [103] N. Bernstein, E.B. Tadmor, Tight-binding calculations of stacking energies and twinnability in fcc metals, *Phys. Rev. B* 69 (9) (2004) 094116.
- [104] A. Ojha, H. Sehitoglu, Critical stresses for twinning, slip, and transformation in Ti-based shape memory alloys, *Shape Mem. Superelast.* 2 (2) (2016) 180–195.
- [105] A. Ojha, H. Sehitoglu, Twinning stress prediction in bcc metals and alloys, *Philos. Mag. Lett.* 94 (10) (2014) 647–657.
- [106] J. Wang, H. Sehitoglu, Twinning stress in shape memory alloys: theory and experiments, *Acta Mater.* 61 (18) (2013) 6790–6801.
- [107] T. Ezaz, H. Sehitoglu, H.J. Maier, Energetics of twinning in martensitic NiTi, *Acta Mater.* 59 (15) (2011) 5893–5904.
- [108] B. Meyer, V. Vanderbilt, Ab initio study of ferroelectric domain walls in PbTiO_3 , *Phys. Rev. B* 65 (10) (2002) 104111.
- [109] B. Karki, P. Müllner, R. Pond, Topological model of type II deformation twinning in 10 M Ni–Mn–Ga, *Acta Mater.* 201 (2020) 604–616.
- [110] B. Li, K.M. Knowles, Molecular dynamics simulation of twinning in devitrite, $\text{Na}_2\text{Ca}_3\text{Si}_6\text{O}_{16}$, *Philos. Mag.* 93 (13) (2013) 1582–1603.
- [111] B. Li, K.M. Knowles, Molecular dynamics simulation of albite twinning and periclone twinning in low albite, *Model. Simul. Mater. Sci. Eng.* 21 (5) (2013) 055012.
- [112] A. Serra, D.J. Bacon, R.C. Pond, Twins as barriers to basal slip in hexagonal-close-packed metals, *Metall. Mater. Trans. A* 33 (13) (2002) 809–812.
- [113] A. Serra, D.J. Bacon, R.C. Pond, Dislocations in interfaces in the h.c.p. metals—I. Defects formed by absorption of crystal dislocations, *Acta Mater.* 47 (5) (1999) 1425–1439.
- [114] M. Gong, G. Liu, J. Wang, L. Capolungo, C.N. Tomé, Atomistic simulations of interaction between basal $\langle a \rangle$ -dislocations and three-dimensional twins in magnesium, *Acta Mater.* 155 (2018) 187–198.
- [115] J. Wang, H. Sehitoglu, H.J. Maier, Dislocation slip stress prediction in shape memory alloys, *Int. J. Plast.* 54 (2014) 247–266.
- [116] J.P. Perdew, K. Burke, M. Ernzerhof, Generalized Gradient Approximation Made Simple, *Phys. Rev. Lett.* 77 (18) (1996) 3865–3868.
- [117] G.L. Clendenen, H.G. Drickamer, Effect of Pressure on the Volume and Lattice Parameters of Magnesium, *Phys. Rev.* 135 (6A) (1964) A1643–A1645.
- [118] J. Goldak, L.T. Lloyd, C.S. Barrett, Lattice Parameters, Thermal Expansions, and Gruneisen Coefficients of Zirconium, 4.2 to 1130 ifm-mode^{circ}/else/textdegree/fi{ }K, *Phys. Rev.* 144 (2) (1966) 478–484.
- [119] E.A. Owen, L. Pickup, XCII. The lattice constants of beryllium, The London, Edinburgh, and Dublin Philosophical Magazine and, *J. Sci.* 20 (137) (1935) 1155–1158.
- [120] S.S. Sidhu, J.C. McGuire, An X-Ray Diffraction Study of the Hafnium-Hydrogen System, *J. Appl. Phys.* 23 (11) (1952) 1257–1261.
- [121] R.W. Lynch, H.G. Drickamer, The effect of pressure on the resistance and lattice parameters of cadmium and zinc, *J. Phys. Chem. Solids* 26 (1) (1965) 63–68.
- [122] W.B. Pearson, CHAPTER VII - TABULATED LATTICE SPACINGS AND DATA OF THE ELEMENTS, in: W.B. Pearson (Ed.), *A Handbook of Lattice Spacings and Structures of Metals and Alloys*, Pergamon, 1958, pp. 123–130.